Ocean Dynamics (2021) 71:1011–1031
https://doi.org/10.1007/s10236-021-01480-x

# Wave characteristics in a semi-enclosed offshore windfarm influenced by East Asian monsoon and extreme weather: a study of central Hangzhou Bay, China

**Bin Yang[1] · Yifan Yang[2] · Zhongliang Yang[3] · Xi Feng[4] · Qing Ye[3] · Liangliang Yu[3] · Jian Ou[1]**

Received: 31 March 2021 / Accepted: 8 August 2021 / Published online: 23 August 2021


**Abstract**
Waves characteristics of the developing windfarm in the semi-enclosed Hangzhou Bay are distinctive due to the East Asian monsoon and frequent typhoons. In this paper, statistical analysis is performed to study the wave parameters in central Hangzhou Bay using 3-year-long wave datasets and the companion wind data. The monsoonal pattern has a significant impact on both annual and seasonal distribution of wave parameters. Compared with mild southeasterlies in summer, the NW-NE winds prevailing in winter tend to produce more extreme waves with large height and spectral energy, and especially in the south of the bay due to the extended fetch. Most waves are generated by local winds and have single-peak spectra. During extreme weather, most large waves had a peak frequency of around 0.2 Hz, i.e., the characteristic frequency. The wave generation processes observed during different extreme events had similar growth-decay tendencies and wave magnitudes. The occurrence probability of significant wave height and mean period can be well represented by both the Weibull and the Rayleigh distribution, and large waves ($H_{1/3} > 1.0$ m, $T_{mean} > 4$ s) occur rarely (2.38% of the time). The correlations between key wave parameters are also examined. In general, this study highlights the typical wind wave patterns and provides practical guidance for future offshore development.

**Keywords** Hangzhou Bay · Wave statistics · Wave spectrum · Monsoon · Extreme weather

## 1 Introduction

The characteristics of surface waves have always been an essential factor for engineering design or risk evaluation in coastal and offshore regions. The vast development of renewable energy has facilitated worldwide constructions of offshore windfarms. For those windfarms and other similar offshore infrastructures, local wave characteristics are essential factors that affect the structural safety and thus need to be carefully evaluated before initializing the project. Considering that ocean waves are irregular and of significant uncertainty, researchers usually apply statistical study and analysis, due to the robustness and practicality of that approach. In the last decade, a large number of statistical and numerical studies have been published addressing various water areas around the world, including Suh et al. (2010), Kumar et al. (2012), Soares and Carvalho (2012), Glejin et al. (2013), Yang et al. (2014), Anoop et al. (2014), Amrutha et al. (2015), Sandhya et al. (2016), Amrutha and Kumar (2017), Nair and Kumar (2017), Shanas et al. (2017, 2018), Chun and Suh (2018), Oliveira et al. (2018), Karmpadakis et al. (2020), and Xiong et al. (2020). Specifically, Suh et al. (2010) analyzed the relationship of deep water wave parameters at the Korean Peninsula using long-term data. Soares and Carvalho (2012) studied the probabilistic distribution of wave heights and periods off the Spanish Coast. Yang et al.

Responsible Editor: Guoping Gao

✉ Yifan Yang
yyan749@aucklanduni.ac.nz

[1] Key Laboratory for Technology in Rural Water Management of Zhejiang Province, Zhejiang University of Water Resources and Electric Power, Hangzhou, China

[2] Department of Civil and Environmental Engineering, The University of Auckland, Auckland, New Zealand

[3] Key Laboratory of Engineering Oceanography, The Second Institute of Oceanography, Ministry of Natural Resources of China, Hangzhou, China

[4] State Key Laboratory of Hydrology, Water Resources and Hydraulic Engineering, Hohai University, Nanjing, China

(2014) studied the statistical variation of wave parameters, spectral pattern, and the characteristics wave groups at the radial sand ridges in the Yellow Sea, using short-term data. Kumar and co-workers paid particular attention to the statistical analysis of wave parameters and spectral patterns of summer monsoon waves on the Indian coast (Kumar et al., 2012; Glejin et al., 2013; Amrutha et al., 2015; Sandhya et al., 2016; Amrutha and Kumar, 2017; George and Kumar, 2019), as well as features in other seasons (Anoop et al., 2014; Nair and Kumar, 2017). Moreover, Shanas et al. (2017, 2018) investigated the sources and wave spectra of waves on the east coast of the Red Sea. Chun and Suh (2018) estimated the wave parameters in the Sea of Japan from wave spectra. Oliveira et al. (2018) discussed the variability of storm wave parameters off the Portuguese coast. Karmpadakis et al. (2020) assessed the wave height distribution in the North Sea using a large dataset. Xiong et al. (2020) studied the statistics of wave heights, pressure, and orbital velocity in the shallow-water inner shelf area of Jiangsu coast, China. Most of these studies adopted a series of similar approaches, including mathematical statistics, regression analysis, and spectral analysis, which have been detailed by Goda (2000), Chakrabarti (2005), and Holthuijsen (2007). A typical statistical analysis of wave parameters involves a wide range of time scales (e.g., by year, season, month, and even day) with an emphasis on the variation and correlation of parameters. The experience of previous studies is beneficial for performing similar research on waves in other areas with different nature.

Hangzhou Bay is a unique water area whose wave features have been significantly understudied in the past decades. Hangzhou Bay locates in the west of the East China Sea, bordering Zhejiang province in the south and Shanghai in the north. The surrounding region contains the world's busiest ports and waterways for cargo shipping as well as some of the longest highway bridges, e.g., Yangshan Port and Donghai Bridge, Hangzhou Bay Bridge, and the Port of Ningbo-Zhoushan. In recent years, a large amount of offshore engineering projects (especially windfarms) are being initiated in middle of the bay, due to the fast economic development in the surrounding cities and the increasing need for clean energy. The construction of new infrastructure requires detailed information of the wave climate to refine the designs. For a long time, Hangzhou Bay has been famous for its unique funnel-shaped inlet, the massive tidal bores, and the semi-enclosed terrain that attenuates a large proportion of swells from open seas. Being influenced by the East Asian monsoon, waves in Hangzhou Bay are generally dominated by wind seas with limited fetch, and thus, an apparent seasonal pattern can usually be observed. The East Asian monsoon is controlled by the sub-tropical high in the Pacific Northwest in summer and the Siberian high in winter, and therefore, the prevalent wind wave directions are often one or the other of two opposites, SE winds/waves in summer and NW winds/waves in winter. This monsoon-related sea state is significantly different from other main monsoon systems around the world (e.g., Indian monsoon) and leads to many disasters along China's coastline (Zhao et al., 2012). Those disasters are caused either by strong cold waves in winter or by tropical cyclones (typhoons) from the East China Sea in summer (Tao et al., 2017); enormous losses of social economy and even human life may follow.

Recently, Yang et al. (2017) reported comprehensive wave features at the Zhoushan Islands, which behave like a barrier at the east entrance of Hangzhou Bay. The observed wave spectra are mainly bimodal due to the presence of both wind waves and swells, and the complex terrain leads to wave directions varying greatly. However, the wave features in Hangzhou Bay are significantly different from those near the Zhoushan Island, because of the complex physical processes, including land shedding, shallow water effect, the diversion of wind and waves, and the fetch restriction. So far, only very limited studies have been done to investigate the wave features in Hangzhou Bay because of financial and technical difficulties in conducting field observations. An early study on waves in Hangzhou Bay (Ru and Jiang, 1985) was based on the visually observed data from the meteorological and hydrological stations in Zhapu, Tanhu, and Youshan. Those sites are located in the northwest, northeast, and south of Hangzhou Bay, respectively. The variation of some key parameters (e.g., wind speed and direction, wave heights, periods, direction) was analyzed based on the annual and seasonal statistics. However, the data of Ru and Jiang (1985) are not systematic and comprehensive enough due to the low frequency of measurement, and the measurement locations were too close to the shorelines to avoid shoaling effects. Generally, the existing research on wave characteristics in central Hangzhou Bay is still far from sufficient to guide engineering practice. This research gap is the motivation of the present study. Considering the urgent need for offshore development in this region, understanding the wave characteristics is obviously essential for further planning, designing, and construction works.

## 2 Data and methodology

### 2.1 Study area and instruments

Figure 1 is a map showing the detailed bathymetry of Hangzhou Bay. The submarine terrain in Hangzhou Bay is generally flat, with some small islands scattered in the center of the bay. Deep troughs can be observed in the northwest near Shanghai and in the east and the southeast near the Zhoushan Islands. Although the bay's opening is generally east-facing, the northeastern part is much more suitable

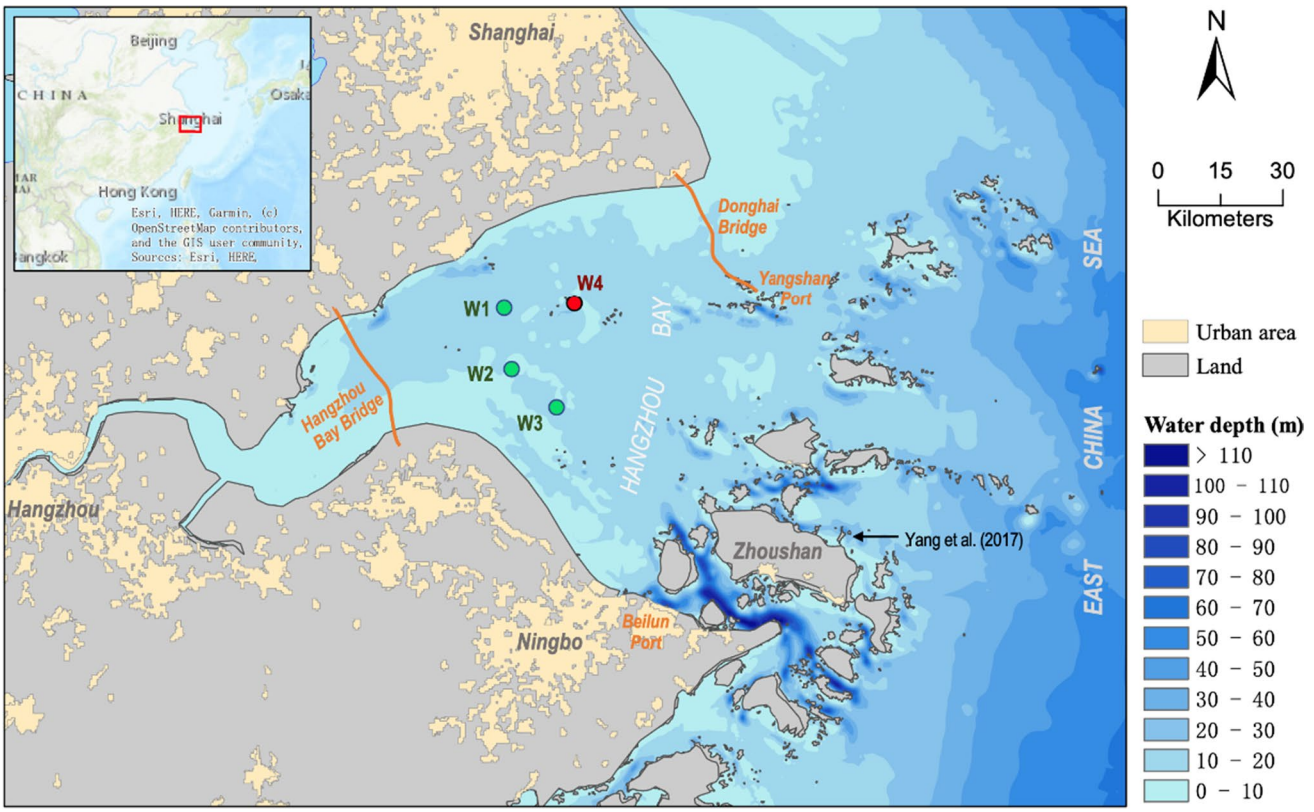


**Fig. 1** Regional map of Hangzhou Bay showing the wave observation stations (W1 ~ W3) and the meteorological station (W4). The location of wave measurements made by Yang et al. (2017) is also marked

for navigation than the southeastern part, which is greatly obstructed by a large number of islands. Hangzhou Bay is influenced by the same monsoon system that prevails in the East China Sea, but the wind direction around the bay may be deflected observably by the complex terrain. Therefore, monitoring real-time wind data is also necessary.

The wave data used in this study were collected by three temporary wave stations located in the center of Hangzhou Bay, as shown in Fig. 1 (green points). The stations are named from north to south and denoted as W1, W2, and W3. The average water depths at the three stations are 10.9 m, 9.8 m, and 10.1 m, respectively. The wind data used in this study were provided by Tanhu Meteorological Station (the red point in Fig. 1), and the observation time was synchronized with measured waves with an observation frequency of 1 h. The meteorological station stands on Tanhu Island located 17.5 km east of W1 and is denoted as W4 in this study. The data of wind speed and direction were measured at 10 m above sea level.

## 2.2 Data collection and processing

Wave profiles were monitored continually for 12 months at each of the wave stations, while the measurement of wind speed and direction was carried out during the entire period. Table 1 shows the detailed start and end dates of measurements at all sites. In total, three separate year-long wave dataset were obtained together with the corresponding wind data. During those observation periods, four major extreme weather events were identified as making the greatest impact at each site, including Typhoon Fung-wong (No. 201416), Typhoon Fitow (No. 201323), Typhoon Danas (No. 201324),

**Table 1** Information of data collection at each station

| Station No | Start date | End date | Data type | Latitude | Longitude |
|---|---|---|---|---|---|
| W1 | 1 April, 2014 | 31 March, 2015 | Wave | 30.607° N | 121.442° E |
| W2 | 1 November, 2012 | 31 October, 2013 | Wave | 30.476° N | 121.469° E |
| W3 | 1 June, 2009 | 31 May, 2010 | Wave | 30.387° N | 121.577° E |
| W4 | Continuous | | Wind | 30.612° N | 121.629° E |

and a strong cold wave in November 2009. Those events are summarized in Table 2. Those three typhoon events were selected for analysis because of their great impacts and the diversity of the path and landfall type. Specifically, Typhoon Fung-wong directly passed through the study area with a landfall; Typhoon Fitow landed in the south of the tested area; and Typhoon Danas passed through the northeastern Pacific in the east of the study area without a landfall. The recorded wave features during extreme weather will be further analyzed and discussed later in this paper.

Waves were monitored at each site using an Acoustic Wave and Current Profiler (AWAC) manufactured by Nortek, which was placed on the seabed to m. The acoustic surface tracking (AST) method was adopted for the measurement (Pedersen and Siegel, 2008). When AST method is not applicable and water depth is less than 15 m, the pressure method (Pedersen and Siegel, 2008) is used to measure the waves synchronously; otherwise, the velocity method (Birch et al., 2004) is used instead. The AWAC instruments were set to measure the wave surface once per hour with a duration of 1024 s, a sampling rate of 2 Hz, and therefore a dataset with 2048 displacement points. The reliability of AWAC instruments have also been tested by Zhou et al. (2020). Although the sampling rate (2 Hz) might cause a portion of the extremely small/short waves to be unidentified, the main parameter ranges of interest (large waves during extreme weather) and the main findings in this study are not affected. Besides, similar sampling strategies have also been examined in some other studies (Kumar et al., 2020; Huang et al., 2021) for long-term wave monitoring.

The raw data obtained were integrated and further processed to calculate a series of key wave parameters using the method of Pedersen et al. (2002). The wave data in each 1024 s were processed as a whole, using the Storm software provided by the manufacturer of the instruments, to calculate the characteristic wave parameters of each hour. The characteristic wave heights of the hour are calculated based on the real-time water surface data and the identified wave crests and troughs. The zero-crossing method was used to calculate each wave period and then derive the characteristic periods of the hour. Then, further long-term wave analysis is based on the data density of one output per hour. The output characteristic parameters include significant wave height $H_{1/3}$ and the corresponding wave period $T_{1/3}$, significant wave height $H_{1/10}$, maximum wave height $H_{\max}$ and the corresponding period $T_{\max}$, mean wave height $H_{\mathrm{mean}}$, and mean wave period $T_{\mathrm{mean}}$. The SUV method proposed by Pedersen et al. (2005) was preferred for calculating wave direction. The fast Fourier transform (FFT) method was used to calculate the frequency spectrum with a degree of freedom of 64. The spectrum high-frequency cutoff is 1 Hz, and the resolution is 0.01 Hz. A number of other spectral wave parameters were also computed for further data analysis and comparison, including mean wave period $T_{01}$ and $T_{02}$, peak period $T_P$ ($T_P = 1/f_p$, where $f_p$ is the spectral peak frequency), the zeroth-order moment $m_0$, the first-order moment $m_{01}$, the second-order moment $m_{02}$, the maximum spectral energy density $S_{\max}$, spectral width $\nu$, and correlation coefficient $R$ (Holthuijsen, 2007). Before further data integration, the abnormal wave data caused by excessive wave surface burrs were deleted. The valid data at W1, W2, and W3 account for 94.5%, 98.0%, and 93.3% of the total data obtained, respectively.

## 3 Annual statistics of wave features

The statistical distribution of key wave parameters at the three different wave stations is generally consistent in this study, due to the flat submarine terrain in central Hangzhou Bay. Table 3 shows the ranges and mean values of some key parameters. Combining all the data at W1 ~ W3, the range is 0.03 ~ 2.21 m for the significant wave height $H_{1/3}$ and 0.05 m ~ 3.21 m for the maximum wave height $H_{\max}$.

**Table 2** Major extreme weather events recorded by different wave stations. Those events made the greatest impact within the year of observation at each site

| Event | Start date | End date | Type | Recorded by |
|---|---|---|---|---|
| Typhoon Fung-wong | 20 September, 2014 | 24 September, 2014 | Landfall | W1 |
| Typhoon Fitow and Danas | 5 October, 2013 | 9 October, 2013 | Landfall (Fitow)<br>No landfall (Danas) | W2 |
| Cold wave | 15 November, 2009 | 18 November, 2009 | – | W3 |

**Table 3** Ranges and mean values of some key wave parameters at three wave stations. The number in the parenthesis is mean values

| Station | $H_{1/3}$(m) | $H_{1/10}$(m) | $H_{\max}$(m) | $T_{\mathrm{mean}}$(s) | $T_P$(s) | $\nu$ | $S_{\max}$ ($m^2$/Hz) |
|---|---|---|---|---|---|---|---|
| W1 | 0.03 ~ 1.81 (0.40) | 0.04 ~ 2.26 (0.50) | 0.05 ~ 3.11 (0.68) | 1.5 ~ 5.4 (2.8) | 1.0 ~ 16.7 (3.6) | 0.19 ~ 0.96 (0.39) | 0.0002 ~ 2.65 (0.15) |
| W2 | 0.05 ~ 1.82 (0.47) | 0.06 ~ 2.23 (0.59) | 0.08 ~ 3.09 (0.81) | 1.5 ~ 6.2 (2.8) | 1.0 ~ 14.9 (3.6) | 0.22 ~ 0.92 (0.40) | 0.0005 ~ 3.35 (0.23) |
| W3 | 0.05 ~ 2.21 (0.47) | 0.06 ~ 2.72 (0.59) | 0.09 ~ 3.21 (0.80) | 1.5 ~ 5.5 (2.9) | 1.1 ~ 16.0 (3.7) | 0.23 ~ 0.85 (0.40) | 0.0009 ~ 5.66 (0.23) |

The mean values are 0.45 m and 0.76 m, respectively. For peak period and mean wave period, the varying ranges are 1.0 s ~ 16.7 s (3.7 s as mean value) and 1.5 s ~ 6.2 s (2.8 s as mean value), respectively. In general, the extreme values of both wave height and wave period are significantly smaller than those observed at the northeast coast of Zhoushan (Yang et al, 2017), where the mean value of $H_{1/3}$ can be two to three times larger with similar water depth.

Despite the general consistency of wave parameters, differences between the wave stations are noticeable. At W1, the annual mean of the significant wave height $H_{1/3}$ and the maximum wave height $H_{\max}$ are observably smaller than the other two sites, while no significant difference in wave periods is found. The extreme wave heights/periods and spectral energy density increase towards the south of the study area (W3). In addition, the consistent peak frequency and spectral width indicate that the shape of wave spectra do not vary significantly in this study. More spectral features will be further discussed in the following sections. Generally, the site-sensitive wave features shown in Table 3 suggest that the location of measurement is also a key factor, as the influence of land proximity is more obvious than in the open ocean.

To further illustrate the sensitivity of wave parameters to the location of measurement, the statistical distributions of wave heights, periods, and wave-wind directions are plotted in Fig. 2 as box charts. Specifically, the outliers beyond the 1.5IQR (interquartile range) are those with relatively low occurrence probability. It can be seen that the correlation between $H_{1/3}$ and $H_{\max}$ are apparent with similar ratios of outliers (see Fig. 2a), although the absolute magnitude of $H_{\max}$ is over 50% greater than $H_{1/3}$. The wave periods show a large number of outliers for peak periods, indicating the presence of long-period swells that propagated into Hangzhou Bay (see Fig. 2b). However, the bay area is still dominated by wind seas in general as the main quartiles (25 ~ 75%) of $T_P$ do not deviate much from those of $T_{\text{mean}}$. More information regarding parameter correlation are further discussed in the discussion section. In Fig. 2c, the wind directions show much greater variability than wave directions, which suggests that the directional wave-wind relationship is not as linear as that in open ocean. The existence of surrounding landform leads to a more complicated pattern of wave generation and propagation.

The real-time wind data are plotted together with the valid wave data in Fig. 3 for further comparison. It is found that the instantaneous variation of wind speed is generally consistent with the trend of significant wave height, as shown by the top subplot of each site. However, the variation of wave height is much less drastic than the wind speed due to the complicated physical air–water interactions, and thus more spikes can be seen for wind speed. The annual mean wind speeds in the observation periods of W1 ~ W3 are 6.5 m/s, 7.2 m/s, and 7.0 m/s, respectively, and the corresponding maximum values are 19.7 m/s, 22.1 m/s, and 22.6 m/s. The existence of long-period energy (evident from the "spikes" of $T_P$ shown in the mid-subplots) proves that the occurrence of swells is evenly distributed across the year and not related to specific types of climate. Furthermore, the subplots of

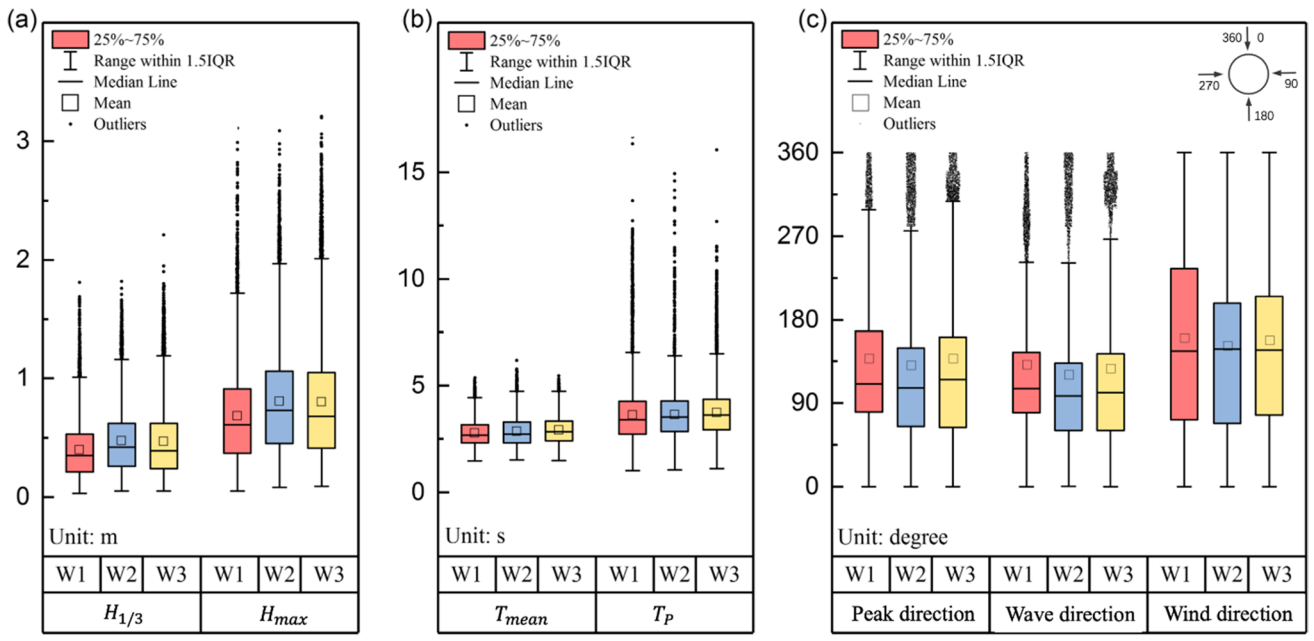


**Fig. 2** Box charts showing the statistical distribution of wave parameters in the study area: **a** wave heights ($H_{1/3}$ and $H_{\max}$); **b** wave periods ($T_{\text{mean}}$ and $T_P$); (**c**) spectrum, wave, and wind directions

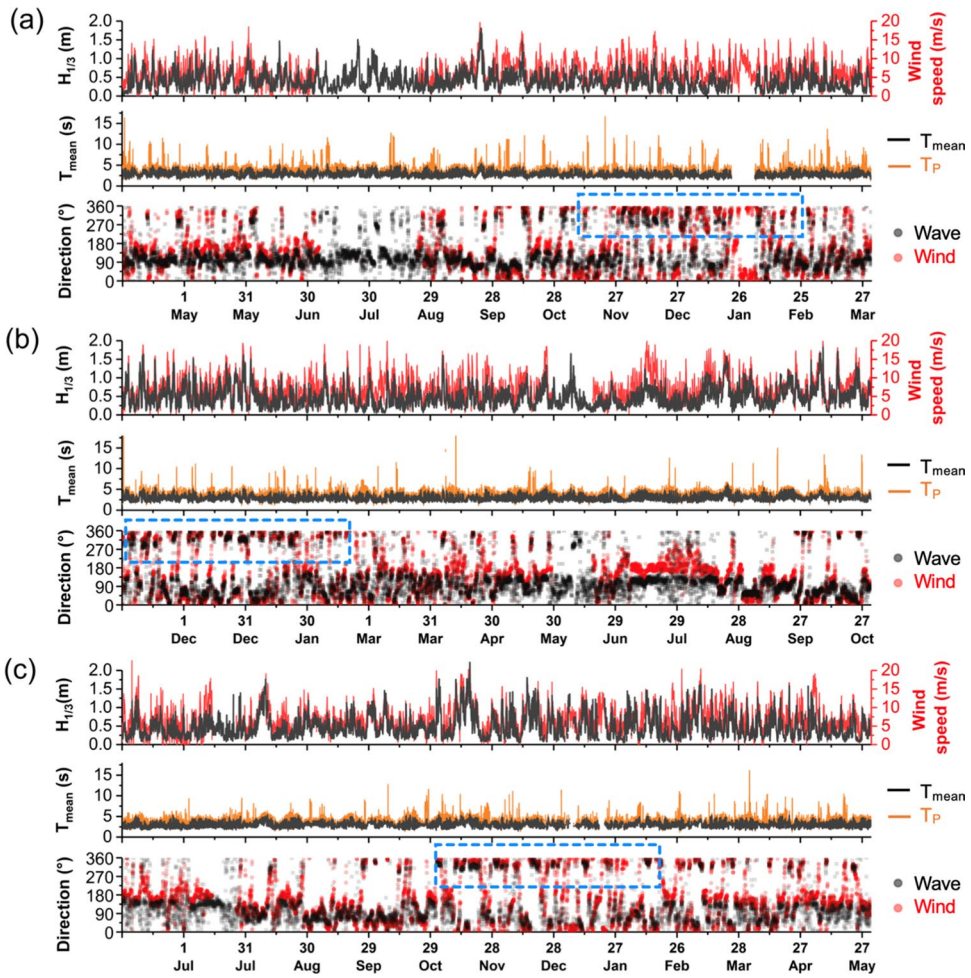


**Fig. 3** Time series plot of all-year data, including significant wave height ($H_{1/3}$), wind speed, peak wave period ($T_P$), mean wave period ($T_{mean}$), and the directions of waves and wind. The subsections include **a** station W1, from 1 April 2014 to 31 March 2015; **b** station W2, from 1 November 2012 to 31 October 2013; and **c** station W3, from 1 June 2009 to 31 May 2010. The dash boxes mark the significant NW-N waves in winter

wind and wave directions also show the more variable wind direction indicated in Fig. 2c. Wind and wave directions often differ during summer, especially at W2. The prevalence of NW-N winds in winter can also be clearly identified (as marked by the dashed-line boxes in Fig. 3).

The detailed correlation between wind direction and wave direction is shown in Fig. 4. It is found in Fig. 4a that the difference between wave stations is small. The general relationship shows a double-asymptotic trend, i.e., NW-NE waves (usually in winter) are more sensitive to the variation of wind direction. Specifically, 0 ~ 40° winds tend to produce waves of 40 ~ 80° direction, 120 ~ 200° winds tend to produce waves of 80 ~ 160°direction, and 320 ~ 360° winds lead to 280 ~ 320° waves. This non-linear directional relationship

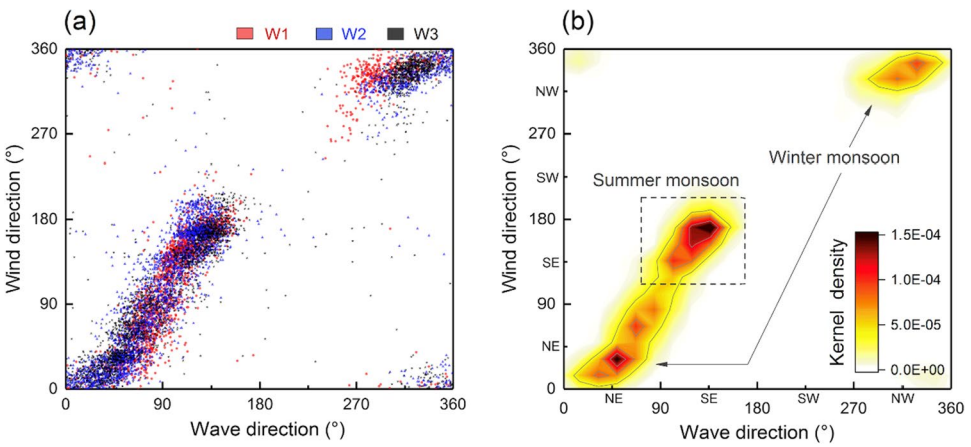


**Fig. 4** The relationship of wave direction and wind direction at three wave stations: **a** scatter plot; **b** kernel density plot showing seasonality

is mainly related to the land terrain of Hangzhou Bay. For example, as the bay inlet is funnel-shaped, and the waves caused by the NW-N winds are deflected further eastward by the terrain (e.g., the upper right corner of the figure). The monsoonal wave pattern is characterized by the absence of S-W waves and multiple regions with high occurrence probability, as shown in Fig. 4b. Compared with the limited directional scatter in summer, the direction of wind waves from the northerly quarter is more variable.

To better characterize the directional distribution of wave events, Fig. 5 shows the occurrence probability and average wave spectral density in different directions. It is found that the occurrence probability at different wave stations is generally consistent (see Fig. 5a). A large proportion of the total waves (67.41%) occurred within NE-SE directions, while only a minimal number of waves (3.55%) occurred within the range of S-WSW. This distribution is in accord with the natural landform of Hangzhou Bay. Waves typically arrive at W1 from directions within ENE-SE, which accounts for 62.76% of total waves, while this number is 56.7% and 52.41% for W2 and W3, respectively. This distinction can be identified in Fig. 5a from the steeper distribution curve of W1. In contrast, waves at W2 and W3 stations are relatively more evenly distributed in the range of NE-SE, accounting for 69.05% and 65.14% of total waves, respectively. Waves from the NE direction at W1 (i.e., 5.7%) are much less frequent than the other two stations (i.e., 12.35% and 12.73%). This difference can be reasonably attributed to the shorter wind fetch from the NE direction at W1 compared to W2 or W3. The effect of the shoreline in the north in limiting the fetch for wave generation from NW-NE directions can also be identified in Fig. 1. In addition, the bathymetry and landform in Hangzhou Bay have noticeable effects on wave propagation from other directions. For example, waves from the western side at W3 are much less frequent than the other two sites due to the shorter fetch, as are waves from the NW-NNW at W1. In general, the directional distribution of wave occurrence at W2 is more suitable to represent the average waves direction in central Hangzhou Bay.

A statistical analysis of the wave occurrence probability from all directions, as shown in Fig. 6, provides a more detailed understanding of the wave distribution at different levels. Waves with $H_{1/3}$ less than 1.0 m occur most of the time at all three stations, so the distribution of their frequencies is similar to the general distribution. Focusing on waves with $H_{1/3}$ equal to 1.0 m or more, it is statistically concluded that at W1, waves mainly arrived from the ENE-SE directions that account for 1.56% of total data, while the other incoming waves account for only 0.42%. Waves higher than 1.0 m at W2 mostly appeared in WNW-SE directions and account for 5.07% of total data, while the W direction accounted for only 0.09%. No waves arrived from

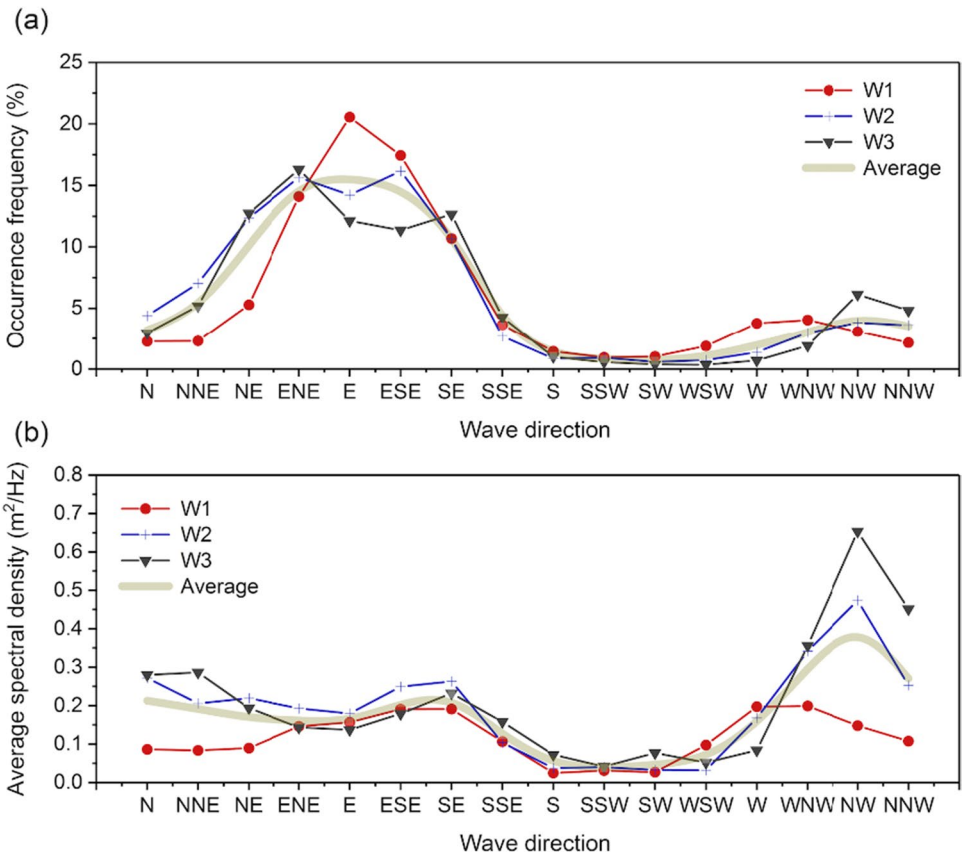


**Fig. 5** Directional distribution of waves at W1, W2, and W3 for **a** occurrence frequency; **b** average spectral density

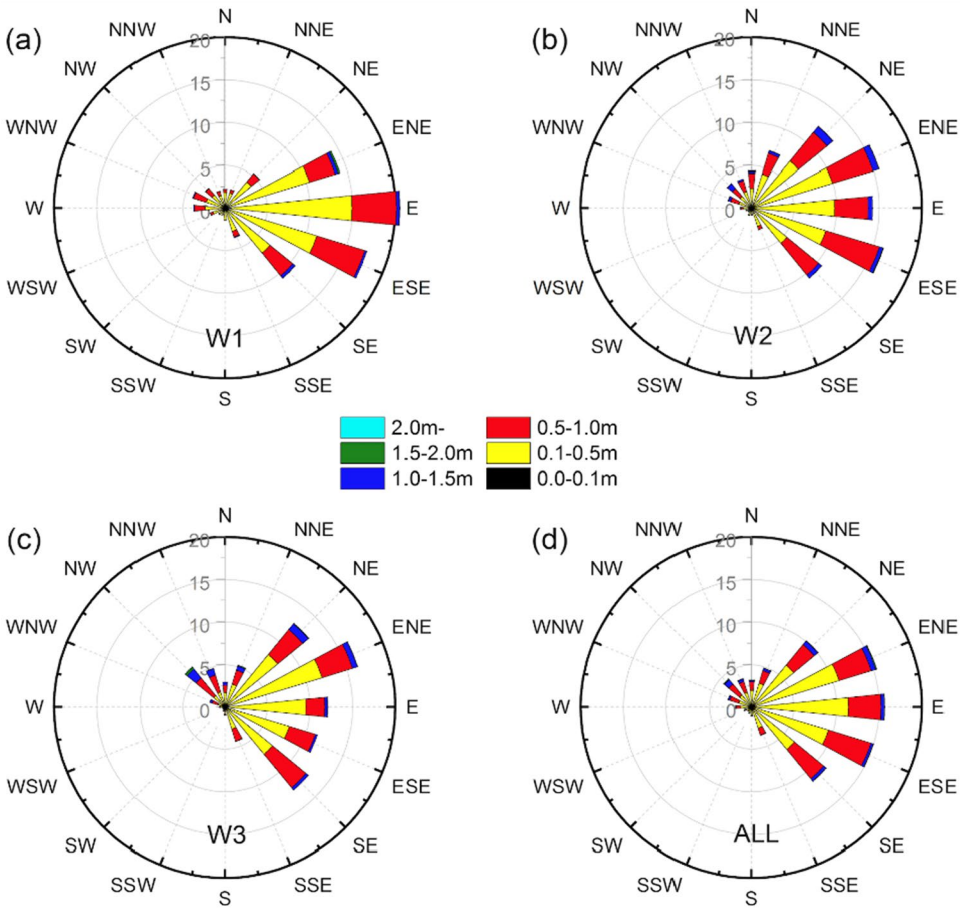


**Fig. 6** Probability rose charts of the wave direction and significant wave height in all levels for **a** station W1, **b** station W2, **c** station W3, and **d** total data in all the wave stations (unit: %)

directions within the range SSE-WSW. The distribution of waves higher than 1.0 m at W3 is generally similar to that at W2, with the majority of waves arriving from WNW-SE directions and account for 6.38% of total data, while the SSE-W waves only account for 0.11%. In general, although a large proportion of total waves are from ENE-SE directions, noticeably high waves events ($H_{1/3} > 1.0$ m) from NW direction are more frequent, particularly at W3. This feature explains the significant peaks of spectral density in Fig. 5b.

## 4 Seasonal variation

As mentioned before, the East China Sea is under the influence of summer and winter monsoons with nearly opposite wind directions. The southeast monsoon usually prevails from May to September every year, due to the subtropical high-pressure zone generated in the northwestern Pacific. In summer, the center of the Pacific high-pressure zone moves closer to the coastline over time, and thus the intensities of wind seas and tidal bores tend to peak in late September (Liang et al., 2016; Li et al., 2019). In contrast, the winter monsoon is driven by the Siberian high and is responsible for the frequent occurrence of cold airs and the consequent massive drops in temperature. In this section, we analyze the characteristics of waves generated in different months of the year to acquire a better understanding of the seasonal wave patterns.

Figure 7 summarizes the distribution of key wave parameters by month, including significant wave height $H_{1/3}$, mean wave period $T_{mean}$, and the maximum wave height $H_{max}$. The monthly means of $H_{1/3}$ show that the values of W1 in winter (November to February) are significantly smaller than other two stations, while this difference in summer becomes minor and uncertain (see Fig. 7a). Similar trends can also be observed in Fig. 7b and c for $T_{mean}$ and $H_{max}$, respectively. This trend is marked by dash boxes in the figure and can be attributed to the monsoons features as mentioned above. As a result, the northwesterly induced waves develop and amplify from W1 to W3, as the fetch length accumulates gradually after leaving the northern shoreline. Typically, more developed wind waves with longer fetch tend to have larger wave heights and periods. In contrast, the predominance of southeasterly in summer, which is much milder, does not differentiate wave parameters at three sites in a significant way.

Figure 8 further displays the monthly distribution of incoming waves of different magnitudes for a better

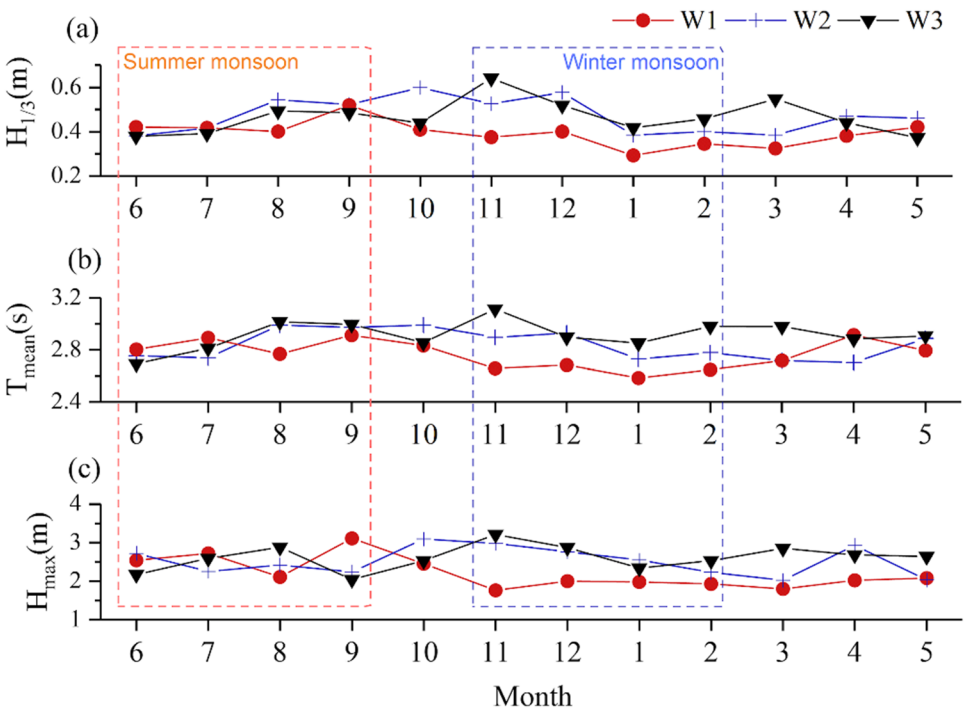


**Fig. 7** Monthly variations of key wave parameters at W1–W3: (**a**) monthly mean significant wave height, (**b**) monthly mean wave period, and (**c**) monthly mean maximum wave height

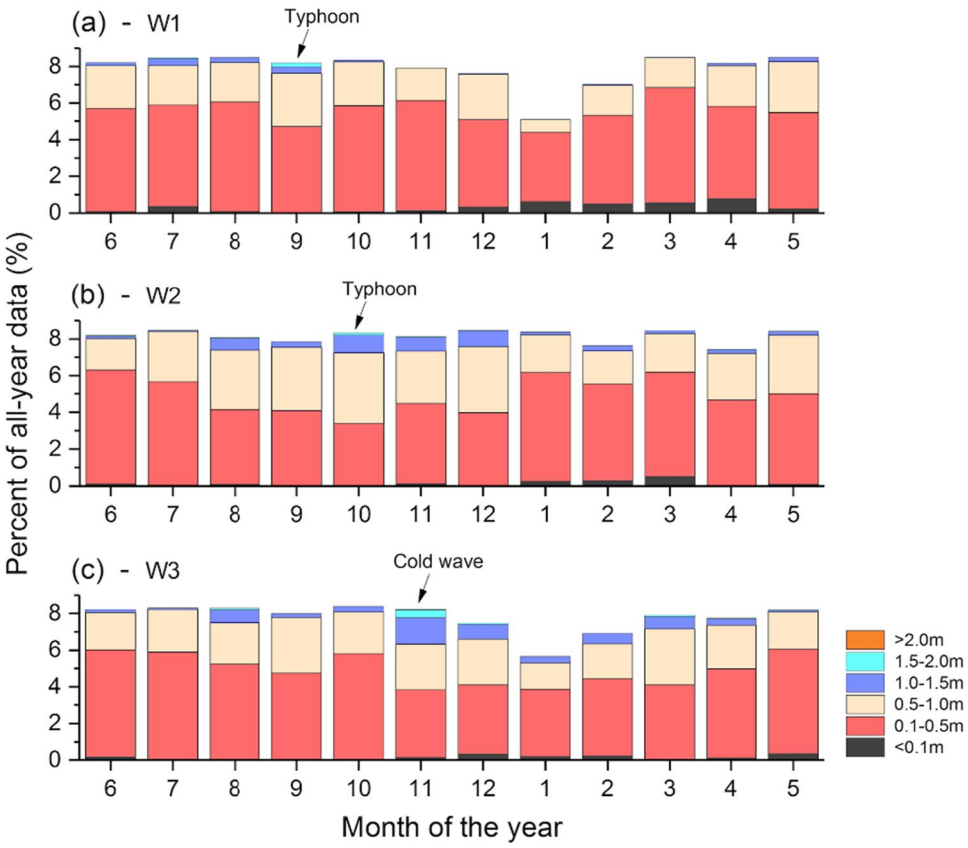


**Fig. 8** Monthly variations of significant wave heights: **a** April 2014 to March 2015 at W1, **b** November 2012 to October 2013 at W2, (**c**) June 2009 to May 2010 at W3

understanding of the joint temporal-spatial wind wave features. It can be found that, at all the three stations, relatively small waves ($H_{1/3}$=0.1 m ~ 1.0 m) account for a large majority of total waves in every month in a year; and this ratio is about 88.4% for all the data combined. However, it should also be noted that, although being much less frequent,

large wave events ($H_{1/3} > 1.0$ m) are more influential to human activities and engineering practices. For example, in winter, fishing activities in Hangzhou Bay are prohibited when the wind speed is larger than about 60 km/h. Although extreme wave events may occur throughout the year, the main driven forces differ. The occurrence of extreme waves from July to September is closely related to the frequent visits of tropical cyclones from the northwestern Pacific. The occurrence probabilities of large wave events in summer at W1 ~ W3 are fairly close, as the sites of measurement are evenly distributed in the middle of the bay. In contrast to summertime, large wave events in winter are basically driven by the cold air from the northwest. Consequently, it can be found in Fig. 8 that large waves observed in winter become more frequent from W1 to W3, which is obviously related to the increase of fetch as mentioned previously. Although the occurrence of extreme weather (tropical cyclones and cold waves) may significantly affect the ratio of large waves in the corresponding months (also marked in Fig. 8), the general trend is not much distorted. The findings above also explain the peak of spectral density displayed in Fig. 5. Although being much less frequent in a year-long period, NW-NE winds emerging in winter tend to be much stronger than the summer monsoon and contribute to most of the large wave events.

The non-uniform distribution of extreme weather across the year also affects the seasonal wave characteristics in Hangzhou Bay. Here, all the large wave events for $H_{1/3} > 1.2$ m at three wave stations are summarized to show the influence of extreme weather at different locations of the bay. Based on the statistical analysis, it is found that over 90% of large waves for $H_{1/3} > 1.2$ m were caused by either typhoons or strong cold waves, while the rest of the large wave events occurred randomly throughout the year without a distinct trend. Thus, 1.2 m is selected as a criterion for further data processing and analysis in this section. The growth and decrease period of each selected event are also analyzed. For a typical typhoon-induced large wave event in open water, the growth period ($T_+$) is usually greater than the decay period ($T_-$). In this study, $H_{1/10} = 0.8$ m was used as the threshold value for determining the start of growth or the end of decay. The fast decay can be attributed to several factors including the dissipation of cyclone energy and the steering of cyclone track. However, this criterion may not be applicable to confined bay areas due to the restricted fetch. The influence of non-extreme or remote cyclones may be much attenuated by the surrounding terrain.

Table 4 summarized the observed large wave events as well as the growth-decay relationship. At W1, all the seven large wave processes were caused by tropical cyclones and were observed between June and October with an average duration of 52 h. The predominant wave directions are E-SE that are consistent with the direction of the bay's inlet. For the other two sites (W2 and W3), the amount of total large waves increases significantly, and the cold wave-related events become much more frequent as the location moves southward. Generally, at W2 and W3, the predominant wave direction in summer shows significant variability due to the randomness of cyclone tracks. Besides, the mean duration of the large wave events decreases from W1 to W3 (i.e. 52 h, 42 h, and 40 h), which indicates the relatively shorter influencing periods of cold waves. Unlike open water areas, no significant dependency is found between the cyclone-related situations and the presence of greater growth period. A majority of the large wave events show a decay period longer than the corresponding growth period.

To summarize, the findings in this section show that the large wave processes in the northern part of Hangzhou Bay (e.g., W1) were mainly caused by tropical cyclones. The impact of NW-NE winds in winter prevails over the summer monsoon and cyclones at W2 and W3, where colder wave-induced extreme waves were observed. The monsoonal pattern, the site location, and the distance to the surrounding shoreline are essential factors for estimating the occurrence and magnitude of extreme waves in a similar confined water area.

## 5 Wave spectrum and composition

The wave spectrum is another robust tool for investigating wave features that might not otherwise be obvious. Statistical wave parameters alone, such as significant wave height, are subject to limitations that might lead to distorted information in terms of available wave energy when wave profiles are not sinusoidal (Coastal Engineering Research Center,

**Table 4** Summary of the observed large wave events for $H_{1/3} > 1.2$ m. The events affected by tropical cyclones occurred within June–October, while the events caused by cold waves occurred within November–April

| Stations | All data | | Affected by tropical cyclones | | | Affected by cold waves | | |
|---|---|---|---|---|---|---|---|---|
| | Total | $T_+ > T_-$ | Total | $T_+ > T_-$ | Dir | Total | $T_+ > T_-$ | Dir |
| W1 | 7 | 4 | 7 | 4 | E-SE | – | – | – |
| W2 | 27 | 6 | 12 | 3 | Vary | 12 | 1 | NW-NE |
| W3 | 26 | 7 | 5 | 2 | Vary | 20 | 5 | NW-NE |

1984). Thus, wave spectrum analysis can determine the composition of observed irregular waves, which are usually the superposition of waves with different periods and directions. For deep water without any fetch restriction, wind waves usually show a single peak, with spectral energy concentrated in a relatively narrow band. In contrast, wind waves combined with swells arriving from outside the generation region are often accompanied by the widening of energy spectra and multiple spectral peaks. For fetch-limited water areas, spectral energy tends to peak more strongly and concentrate around the peak frequency (Hasselmann et al., 1973; Holthuijsen, 2007). The data in this study show that wave spectra in Hangzhou Bay are generally dominated by well-defined single-peaked spectra. Multi-peak spectra could also be observed occasionally with relatively small wave heights. For data at all the three stations combined, single-peak spectra accounted for over 80% of the total waves observed (81.7%, 88.0%, and 82.7% at W1 ~ W3, respectively). The prevalence of single-peak mode indicates that the influence of swells in Hangzhou Bay is relatively minor, which is apparently due to the semi-enclosed nature of the bay. Figure 9 shows a series of typical single- and multi-peak spectra measured at different sites. The largest peak energy density was observed at W3 during the large cold wave in 2009 (see Fig. 9a). The spectral shapes observed during tropical cyclones and cold waves are highly similar with the peak frequencies around 0.2 Hz.

More detailed information about the spectral features in different months is shown in Fig. 10. Generally, the maximum monthly spectral densities are consistent in summer, but a significant difference can be observed in winter (see Fig. 10a). The distinct peak of W3 in November 2009 is due to the strong cold wave that is also shown in Fig. 9a. Besides the peak of energy density, the spectral width at W3 in winter is also significantly larger than other two site. An explanation is that the wind waves generated in the north of the bay are subject to spectral energy dispersion when propagating southward, and therefore, more various wave components are integrated at W3. Presumably, higher energy density and wider spectra can be observed in winter at further southeast where it is close to Zhoushan Island. Combining the data in both Figs. 10a and b, it can be inferred that, in wintertime dominated by cold airs of NW-NE directions, the general spectral density is generally correlated to the spectral width in central Hangzhou Bay. In contrast, no noticeable dependency is found in summer.

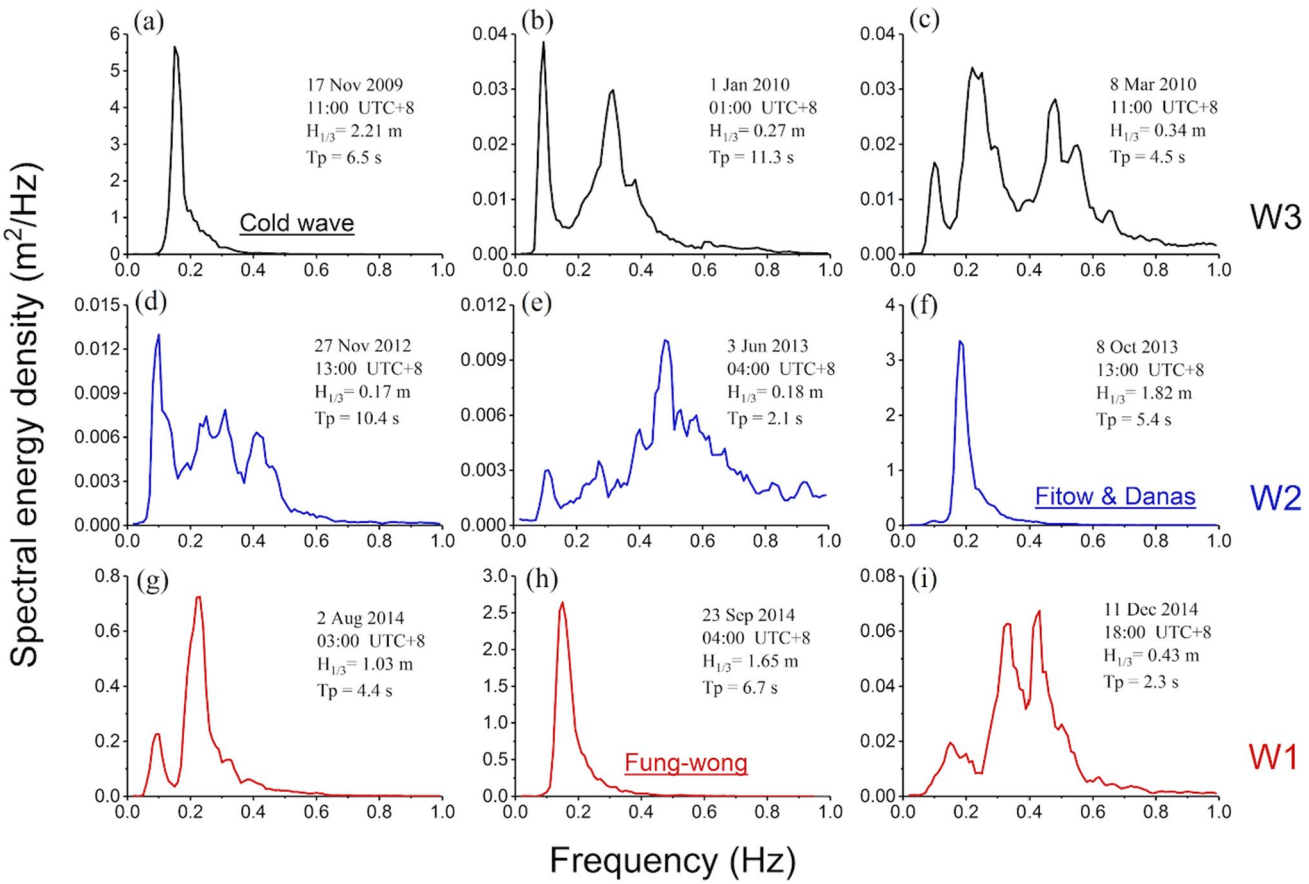


**Fig. 9** Typical single-peak and multi-peak spectra measured at all the three wave stations

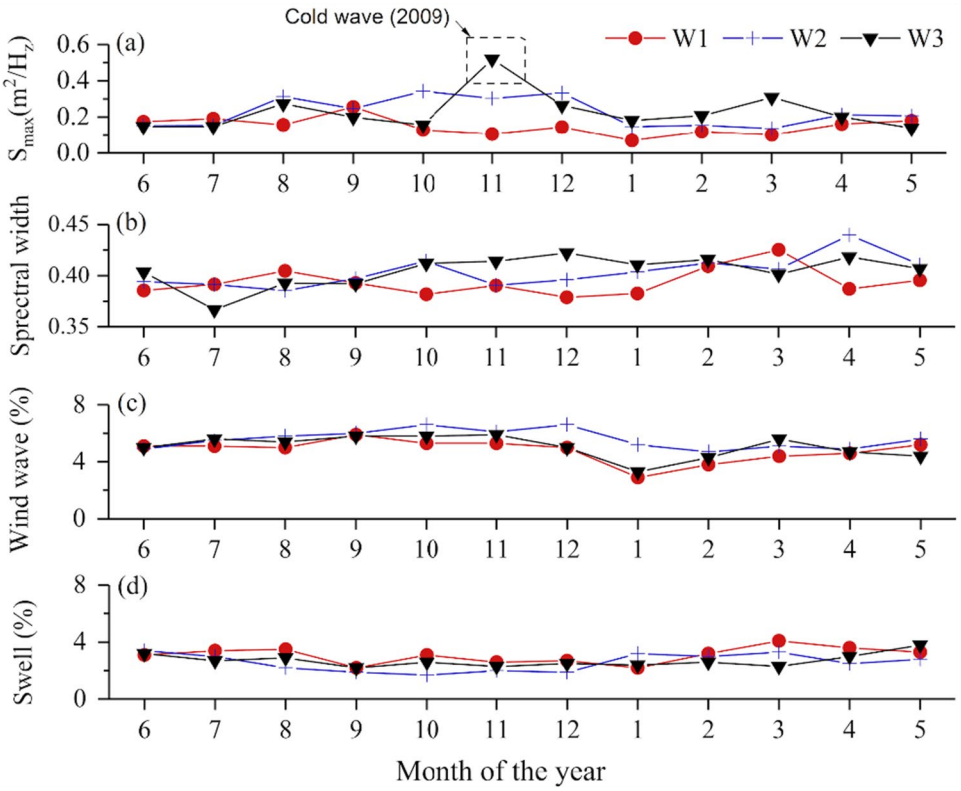


**Fig. 10** Variation of **a** monthly average maximum energy density, **b** monthly average spectral width υ, **c** monthly occurrence of wind waves, and **d** monthly occurrence of swells

To better categorize the specific composition of observed waves, the method proposed by Portilla et al. (2009) is applied to estimate the proportion of wind waves and swells. The ratio of the measured peak to the peak of the fully developed P-M spectrum (Pierson and Moskowitz, 1964) at the corresponding frequency is used as a criterion, i.e., > 1 for wind waves and < 1 for swells. According to the results, wind waves account for 61.8% of the total waves observed (57.6%, 67.1%, and 60.8% at W1 ~ W3, respectively). The monthly variations of the proportions of wind waves and swells are shown in Figs. 10c and d. It can be seen that the site-specific proportions of wind waves in different months are fairly close with consistent trends, except for the data of W1 and W3 in January (see Fig. 10c). This significant drop is due to some invalid data sections. Therefore, it can be concluded that the wave composition in central Hangzhou Bay does not vary drastically with location and season.

Further analysis shows that, for wind waves separated from the observed data, the significant wave height ranges from 0.06 to 2.21 m with a mean of 0.54 m. The magnitude of swells is much smaller with a range of 0.03 ~ 1.57 m and the mean of 0.27 m. However, the mean periods of measured wind waves and swells are very close (about 2.8 s) and are much smaller than the mean peak period of swells (4.3). This contrast indicates that the swells in Hangzhou Bay are mostly less propagated young swells, which is obviously due to the spatial restriction in the semi-enclosed region. For the relatively large waves with $H_{1/3} > 1$ m, wind waves account for 97.3% of the total waves observed (98.1%, 98.6%, and 96.0% at W1 ~ W3, respectively), while, using another criterion, the proportion of single-peak waves is 98.5% (97.5%, 100%, and 97.6% at W1 ~ W3, respectively). The prevalence of wind waves and the single-peak mode are highly correlated in this study for large wave events. Therefore, more attention regarding design safety and potential maritime hazards shall be paid particularly to extreme weather (e.g., tropical cyclones and cold waves) that can cause massive and long-lasting occurrences of winds.

## 6 Wave development during extreme weather

This section further analyzes and discusses the growth and decay of large waves during extreme weather, i.e., typhoons and cold waves. As mentioned in the previous section, the East China Sea is periodically influenced by the tropical cyclones from the Pacific Northwest in summer and cold airs from East Siberia in winter. The impact of typhoons is subject to great variability due to the uncertainty of cyclone tracks, while the direction of cold airs is relatively stable. Thus, in this study, two typhoon events were selected for analysis: one typhoon (Fung-wong) that directly passed Hangzhou Bay and two typhoons (Fitow and Danas) that

approached the East China Sea from different directions almost simultaneously. The strong cold wave observed in November 2009 is also analyzed for comparison. More detailed information about these events is given in Table 2. The individual tracks of these tropical cyclones are shown in Fig. 11. Because of the Coriolis effect, those tropical cyclones rotate counterclockwise in the Northern Hemisphere, which is a key factor determining the directions of winds and waves.

Figure 12 displays the time series plots of wave heights ($H_{1/3}$ and $H_{max}$), wave periods ($T_{mean}$ and $T_P$), and the direction of waves/wind at three different sites during the few

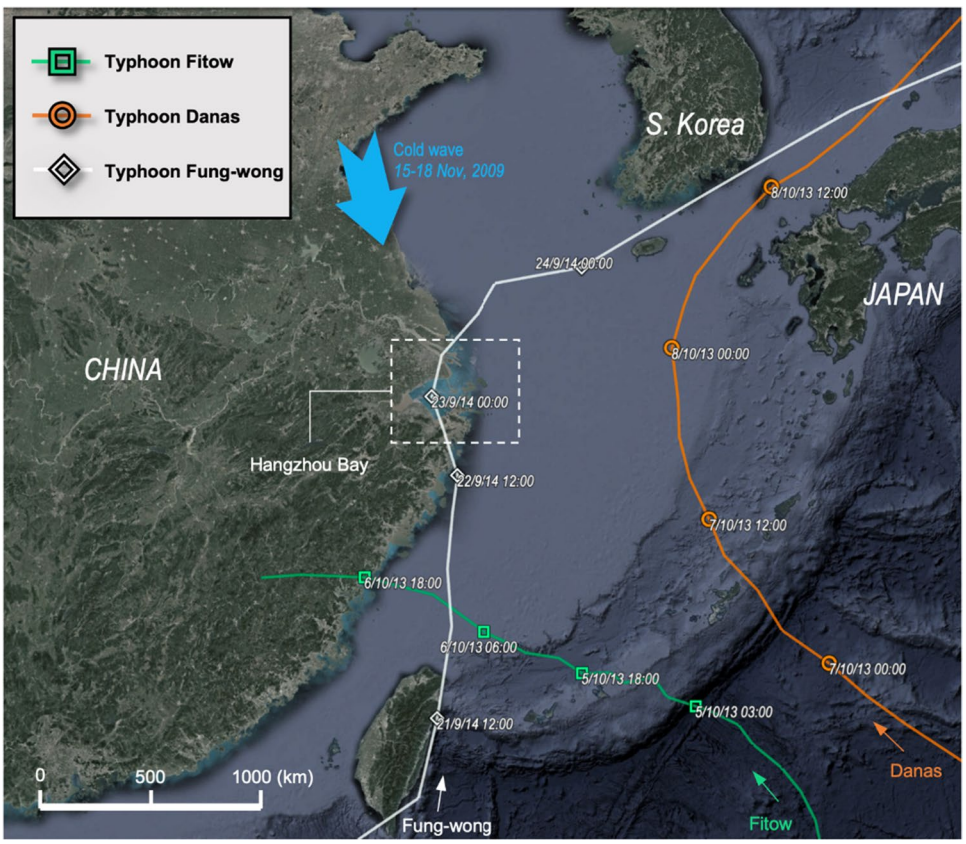


**Fig. 11** Path of typhoon **a** Fung-wong, **b** Fitow, and **c** Danas

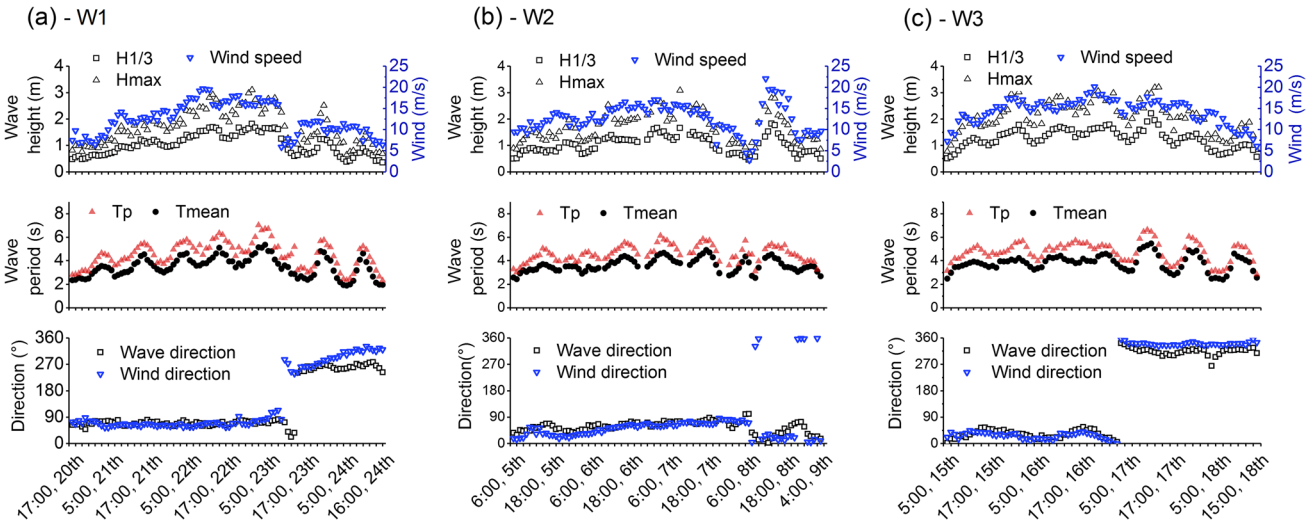


**Fig. 12** Time series plots of wave heights, periods, and directions for measured data at **a** station W1 between 20 and 24 September, 2014; **b** station W2 between 5 and 9 October, 2013; and **c** station W3 between 15 and 18 November, 2009

days of each of the events in Table 2. It can be seen that $H_{1/3}$ and wind speed are highly correlated with consistent trends (see subplots on top). Regression analysis shows that both $H_{1/3}$ and $H_{max}$ are linearly related to wind speed in general with the scale ratios of 0.087 and 0.145 and that those ratios do not change with location or specific type of climate. The measured wave heights are significantly lower than the theoretical heights of fully developed wind waves (Holthuijsen, 2007). These findings reveal that the development of wind waves was limited by both fetch restriction and water shallowness. Besides, the $H_{1/3} - H_{max}$ and $T_{mean} - T_P$ relationships show fair consistency with time, and their correlations will be further analyzed in the following sections. It should also be noted that the wave periods data in Fig. 12 show periodical oscillation with time, which is probably due to the influence of the tidal period. Preliminary analysis shows that the oscillations at each site are not entirely consistent with each other and are also not entirely consistent with the tidal period. The detailed mechanism is very complicated and beyond the scope of the present study. Such oscillation only occurred to wave period data, and no significant effect on wave height data has been observed. Thus, the main findings and conclusions in this study are not affected.

Note: [a]Typhoon Fitow.

[b]Typhoon Danas.

[*]*WW* wind wave.

[**]*SP* single-peak spectrum.

Table 5 summarizes the key wave parameters during the entire growth-decay period of the selected extreme weather events. For waves at W1 during Typhoon Fungwong, $H_{1/3}$ increased from 0.48 to 1.81 m in 56 h and then quickly decreased to 0.49 m in 28 h (see Fig. 12a). A transition of the predominant wind direction from NNE to W was observed as the northbound cyclone approached, arrived, and left Hangzhou Bay. Station W2 consecutively recorded the wave processes of Typhoon Fitow and Danas, which affected Hangzhou Bay from a distance in the south and the east, respectively. During Typhoon Fitow, $H_{1/3}$ increased from 0.5 to 1.66 m in 45 h and dropped to 0.46 m quickly in 28 h after landfall (see Fig. 12b). The predominant wave direction (from NE to ENE) concurs with the cyclone's counterclockwise rotation. The impact of Typhoon Danas was observed immediately after Typhoon Fitow with a much shorter duration (i.e., 7-h growth and 8-h decay) because of the typhoon's remoteness from the site. During this process, the maximum value of $T_{mean}$ (4.6 s) is observably smaller than other events, and the proportion of multi-peak spectra increased to 50%. Comparing the calculated parameters of the three typhoon events, it is found that the ratio of $T_+/T_-$ and the spectral composition are both reasonable indicators of the impact of cyclones, while the latter is more suitable for the study area. The limitation of using $T_+/T_-$ as a criterion has also been discussed previously in this study. Compared with the wave development during typhoons, no significant difference is found for the cold wave. At W3, $H_{1/3}$ increased from a 0.51 to 2.21 m in 55 h and then decreases to 0.56 m in 28 h (see Fig. 12c). This process resembles those typhoon-related events in terms of both wave heights and wave periods. The predominant wind/wave directions vary within the range of NE-NW, which are too some extent similar to that for tropical cyclones. Despite the basic mechanism of typhoons and cold waves being entirely different, the corresponding large wave events generally follow the same mode of development. This similarity may help to reduce the potential complexity for engineering design and other activities.

It is also noticed in Table 5 that the proportion of wind waves is usually higher than waves of single-peak spectra, probably because a portion of the wind waves interacted with swells. This difference is also closely related to the fetch location and local topography and involves a complicated sea-state mechanism that needs more study in the future.

In previous sections, it is mentioned that the observed wave spectra during large wave events were dominated by single-peak spectra. Figure 13 shows more detailed information about the temporal development of spectral energy distribution during the selected events. It can be seen that the peak frequency generally fluctuates around 0.2 by up to 0.05 Hz. Besides the high-energy zone at W3 observed around midday on the 17th, the temporal and spatial distribution of the spectra is generally consistent with similar widths. As the analyzed types of extreme weather are the main sources of maritime hazards, 0.2 Hz can be reasonably treated as the characteristic frequency in Hangzhou Bay for evaluating potential wave-related damages or risks

**Table 5** Key wave parameters during the growth and decay of the selected extreme weather events

| Stations | $H_{1/3}$(m) | | | $T_{mean}$(s) | | | Duration (h) | | Wave direction | Ratio (%) | |
|---|---|---|---|---|---|---|---|---|---|---|---|
| | Before | Max | After | Before | Max | After | $T_+$ | $T_-$ | | WW[*] | SP[**] |
| W1 | 0.48 | 1.81 | 0.49 | 2.4 | 5.4 | 2.0 | 56 | 28 | NNEW | 96.4 | 95.2 |
| W2[a] | 0.50 | 1.66 | 0.46 | 2.5 | 4.9 | 2.5 | 45 | 28 | NEENE | 98.4 | 87.5 |
| W2[b] | 0.46 | 1.82 | 0.50 | 2.5 | 4.6 | 2.7 | 7 | 8 | NENENNE | 81.0 | 50.0 |
| W3 | 0.51 | 2.21 | 0.56 | 2.5 | 5.5 | 2.5 | 55 | 28 | NNENNWNW | 100 | 100 |

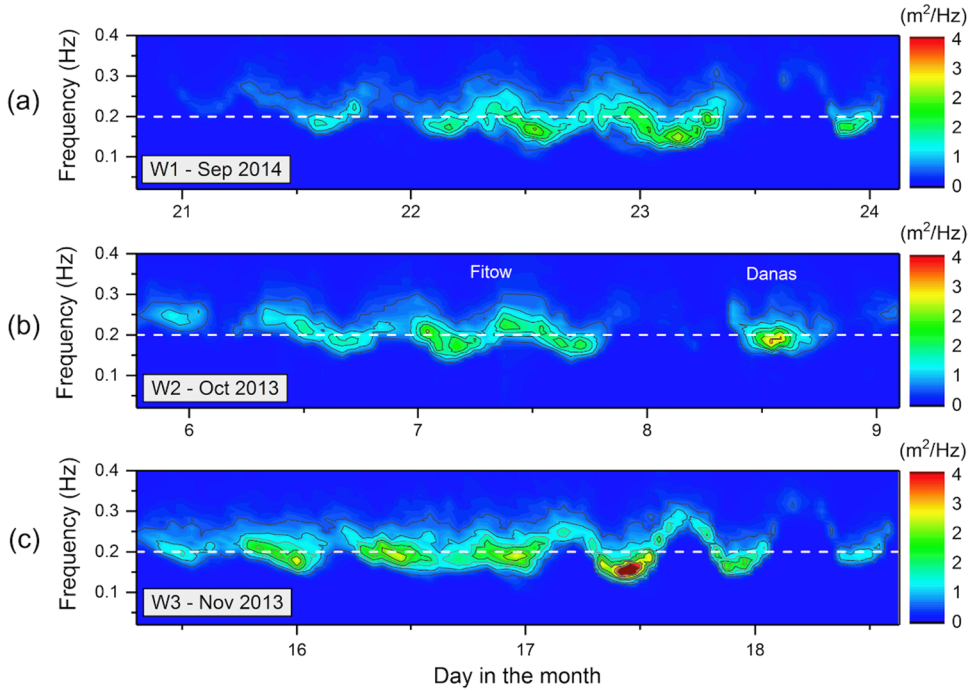


**Fig. 13** Real-time distribution of spectral energy density: **a** W1 during Typhoon Fung-wong, 20 ~ 24 September, 2014; **b** W2 during Typhoon Fitow and Danas, 5 ~ 9 October, 2013; and **c** W3 during a strong cold wave, 15 ~ 18 November, 2009 (unit: $m^2$/Hz)

(e.g., sympathetic vibration). As an example, Ruzzo et al. (2019) investigated the wave impact on offshore wind turbines using spectral analysis regarding the natural frequency, response spectra, and hydrodynamic damping ratios. More applications can be well designed based on the findings in this study.

## 7 Discussion

### 7.1 Wave joint distribution

A holistic understanding of wave parameters is valuable for practitioners. The joint distributions of significant wave height $H_{1/3}$ and mean wave period $T_{mean}$ at the wave stations are generally consistent, as shown in Table 6. The most frequent waves are those with a significant height of 0.1 ~ 0.5 m and the period of 2 ~ 3 s. Waves with $H_{1/3} = 0.1 \sim 1.0$ m and $T_{mean} = 2 \sim 4$ s occur about 70 ~ 80% of the time, at all of the three wave stations. Comparatively, more waves with greater mean period and significant wave height can be observed in the southern part of the bay, i.e., W3 relative to W1. This trend is consistent with our previous conclusion that the limited northerly fetch length at W1 impedes the development of large waves, as those waves are basically caused by NW-NE winds in winter. Waves with $T_{mean} > 6$ s occurred only once at W2, with a mean wave period of 6.2 s, a significant wave height of 1.39 m, and a southeasterly direction of arrival. Thus, the occurrence of such waves is negligible and not discussed particularly in this study. For large waves with $H_{1/3} > 1.0$ m at all the three sites, the mean period ranges from 2.3 to 6.2 s with a mean of 3.9 s. For the waves with $T_{mean} > 4$ s, the significant height ranges from 0.08 to 2.21 m with a mean of 0.82 m. In this study, we suggest that only

**Table 6** Joint distribution of occurrence probability of significant wave height and mean wave period (unit: %)

| $H_{1/3}$(m) | $T_{mean}$(s) at W1 | | | | | $T_{mean}$(s) at W2 | | | | | $T_{mean}$(s) at W3 | | | | |
|---|---|---|---|---|---|---|---|---|---|---|---|---|---|---|---|
| | 1 ~ 2 | 2 ~ 3 | 3 ~ 4 | 4 ~ 5 | 5 ~ 6 | 1 ~ 2 | 2 ~ 3 | 3 ~ 4 | 4 ~ 5 | 5 ~ 6 | 1 ~ 2 | 2 ~ 3 | 3 ~ 4 | 4 ~ 5 | 5 ~ 6 |
| < 0.1 | 0.87 | 2.36 | 0.43 | 0.01 | - | 0.18 | 1.23 | 0.11 | - | - | 0.11 | 1.11 | 0.40 | - | - |
| 0.1 ~ 0.5 | 6.83 | ***44.29*** | 11.82 | 0.70 | 0.01 | 7.80 | ***38.80*** | 10.32 | 1.16 | 0.01 | 4.37 | ***39.55*** | 12.27 | 1.24 | - |
| 0.5 ~ 1.0 | - | 10.40 | 12.39 | 2.45 | - | 0.01 | 14.18 | 15.73 | 3.22 | 0.07 | - | 10.02 | 14.99 | 2.68 | 0.07 |
| 1.0 ~ 1.5 | - | 0.03 | 0.91 | 0.78 | 0.02 | - | 0.21 | 2.81 | 1.67 | 0.18 | - | 0.48 | 3.48 | 1.79 | 0.05 |
| 1.5 ~ 2.0 | - | - | 0.11 | 0.09 | 0.03 | - | - | 0.03 | 0.21 | 0.05 | - | 0.01 | 0.16 | 0.45 | 0.09 |
| > 2.0 | - | - | - | - | - | - | - | - | - | - | | | | | 0.01 |
| Total | 7.69 | 57.09 | 25.66 | 4.03 | 0.07 | 7.99 | 54.42 | 29.0 | 6.26 | 0.31 | 4.5 | 51.2 | 31.3 | 6.2 | 0.2 |

waves show both $H_{1/3} > 1.0$ m and $T_{mean} > 4$ s are the rare large waves of interest, and those waves occur only 2.38% or less of the time at all three wave stations.

Figure 14 shows the cumulative probability distributions of significant wave height $H_{1/3}$ and mean wave period $T_{mean}$ at three wave stations and those of the combined dataset. It can be seen in Fig. 14a that, at W1, the proportions of small and large waves are slightly higher than the other two sites, probably due to the northmost location. Generally, the trends of $H_{1/3}$ at three sites are very similar, and thus, the distribution of the combined dataset in Fig. 14d can represent the entire region. The same similarity can also be found in Fig. 14e–h for mean wave period data.

To better summarize the wave climate of central Hangzhou Bay, the occurrence distributions of $H_{1/3}$ and $T_{mean}$ are analyzed both jointly and separately, as shown in Fig. 15, with all the data combined. In Fig. 15a, the joint distribution of $H_{1/3}/\overline{H_{1/3}}$ and $T_{mean}/\overline{T_{mean}}$ is represented by a kernel density estimation plot, in which a darker region stands for greater occurrence probability. What the unit of a kernel density plot stands for depends on the size of the output cell, but the relationship of occurrence probability between different areas is not affected. It can be seen that most of the data are concentrated in the region for $H_{1/3} < \overline{H_{1/3}}$ and $T_{mean} < \overline{T_{mean}}$. The spreading of the scatters along $X$- and $Y$-axis is generally symmetric with larger $H_{1/3}$ and $T_{mean}$. The probability of waves appearing outside the 0.02 contour line is less than 1% of that inside the line for 1.6. As mentioned before, each data point represents the characteristic wave parameters in a duration of 1024 s that was measured once per hour. Figures 15b and c analyze the separate cumulative probability distribution of $H_{1/3}$ and $T_{mean}$, respectively. The equations of Rayleigh distribution, Weibull distribution, and Gamma distribution are applied to fit the measured data.

It is found that, for significant waves heights, Rayleigh and Weibull distributions show similar and good accuracy for waves higher than the 10th percentile group compared with Gamma distribution. For mean wave periods, the performance of the Weibull distribution is slightly better. It is also noticed that even Weibull distribution will lead to a significant overestimation for small/short waves regarding both $H_{1/3}$ and $T_{mean}$, which can be identified by the deviation of red trend lines in Figs. 15a and b. This is possible due to that the measurement instruments might overlook some information of small/short waves because of their sampling frequency (2 Hz). However, this inaccuracy will not affect the main findings in the present study that mainly focuses on large/long waves in extreme weather. In general, the Weibull distribution provides the best accuracy for the parameter ranges of interest.

As the Weibull distribution is usually applied for truncating the unrealistic wave heights of the Rayleigh distribution in shallow water (Battjes and Groenendijk, 2000; Mai et al., 2011; Wu et al., 2016), it is inferred that the shallow water effect in the central Hangzhou Bay is not significant. However, the abovementioned trend is only for $H_{1/3}$ and $T_{mean}$ that represent the general seas state; the occurrence of extremely large waves might be subject to more complicated conditions. Further analysis is needed in the future to investigate the wave hydrodynamics in this area.

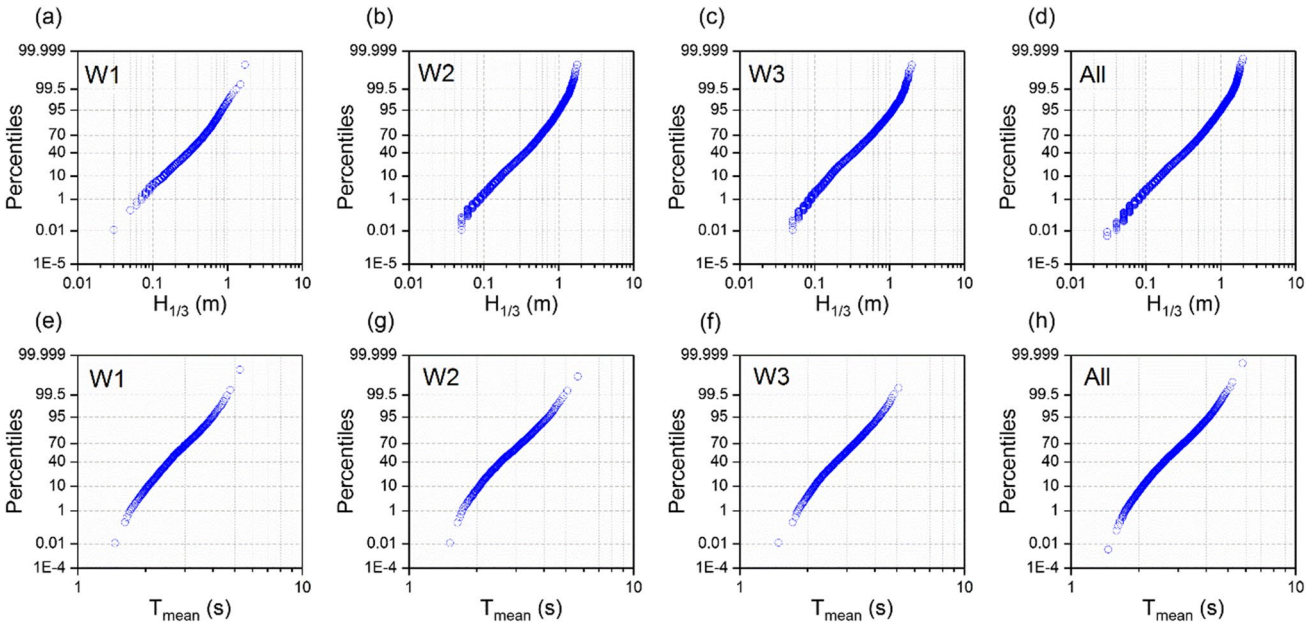


**Fig. 14** Cumulative probability distributions of significant wave height and mean wave period at three wave stations (W1–W3) and those of the combined dataset

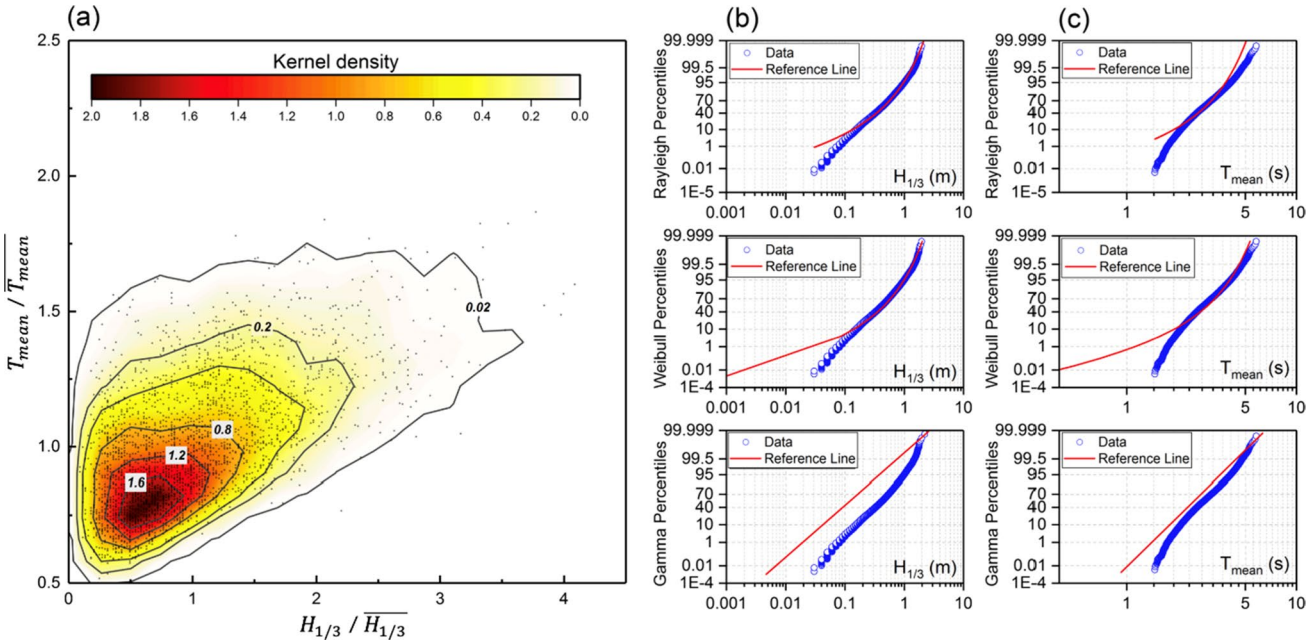


**Fig. 15** Probabilistic distribution of $H_{1/3}$ and $T_{\text{mean}}$: **a** the joint distribution of $H_{1/3}/\overline{H_{1/3}}$ and $T_{\text{mean}}/\overline{T_{\text{mean}}}$; **b** fitting of the cumulative probability of $H_{1/3}$; **c** fitting of the cumulative probability of $T_{\text{mean}}$. The fitted equations include Rayleigh, Weibull, and Gamma distributions

## 8 Correlation between wave parameters

The statistical wave heights, as derived by Longuet-Higgins (1952), can generally be represented by the superposition of a large number of normally distributed random waves that are grouped in a single narrow band of frequencies. Because the length of a vector with Gaussian distributed components basically follows the Rayleigh distribution, wave heights can be approximated using a group of wave spectral parameters, including the zeroth-order moment $m_0$, the first-order moment $m_{01}$, and the second-order moment $m_{02}$. For example, $H_{1/3} \approx 4\sqrt{m_0}$ is usually used for deep water waves when only wave spectra are available. The assumption that wave heights are Rayleigh distributed makes it possible to derive specific relations between wave parameters, e.g., $H_{\max} \approx 1.52H_{1/3}$, $H_{1/3} \approx 1.598H_{\text{mean}}$, etc. More detailed relations can be referred to in Goda (2000). Similar to wave heights, wave periods may also be estimated by spectrum-based equivalents, e.g., $T_{01}$ and $T_{02}$, which are calculated using corresponding spectral moments. However, the Rayleigh distribution is based on idealized conditions and may not be suitable for coastal regions; therefore, discretion should be exercised when examining the results.

In this study, we analyzed the statistical features of the total data and derived the detailed correlation between key wave parameters, as shown in Fig. 16. The main purpose is to examine how much the wave correlations in a semi-enclosed bay area differ from those in an idealized open ocean. It was found in Fig. 16a, b, and c that there is a good linear relationship between he measured significant wave height $H_{1/3}$ and other wave heights ($H_{\max}$, $H_{1/10}$, and $H_{\text{mean}}$). Specifically, regression analysis shows that the ratio of $H_{\max}/H_{1/3}$ in this study is around 1.70, which is higher than the value (1.65) in the south of the radial sand ridges near the Jiangsu coastline of China (Yang et al., 2014), the value (1.65) near India's coast (Kumar et al., 2011), and the theoretical value (1.52) of the Rayleigh distribution (Longuet-Higgins, 1952). The design criteria (1.80) proposed by Goda (1974) for breakwaters are still capable of providing sufficient safety redundancy. The ratios of $H_{1/10}/H_{1/3}$ and $H_{1/3}/H_{\text{mean}}$ in this study are 1.256 and 1.571, respectively, which are in accord with the theoretical values (1.271 and 1.598) of the Rayleigh distribution, as shown by the blue lines in Fig. 16b and c. The trends displayed in Fig. 16a indicate that the extreme large waves were amplified when propagating within Hangzhou Bay. In contrast, the ratio of $H_{1/3}/\sqrt{m_0}$ ($\approx 3.69$, see Fig. 16g) in this study is significantly smaller than the theoretical value (4.0), suggesting the attenuation of wave heights in such a shallow bay area with fetch restriction. This value (3.69) is also marginally smaller than that (3.72) proposed by Kumar et al. (2011) and the value (3.75) of Yang et al. (2014). The opposite comparisons in Fig. 16a and g imply that the funnel-shaped inlet of Hangzhou Bay may to some degree amplify the extreme large waves. This unique shape is responsible for the accumulation and amplification of wave energy, which is also the main driving force of the Qiantang River tidal bore. Xu et al. (2018) simulated the energy amplification process in

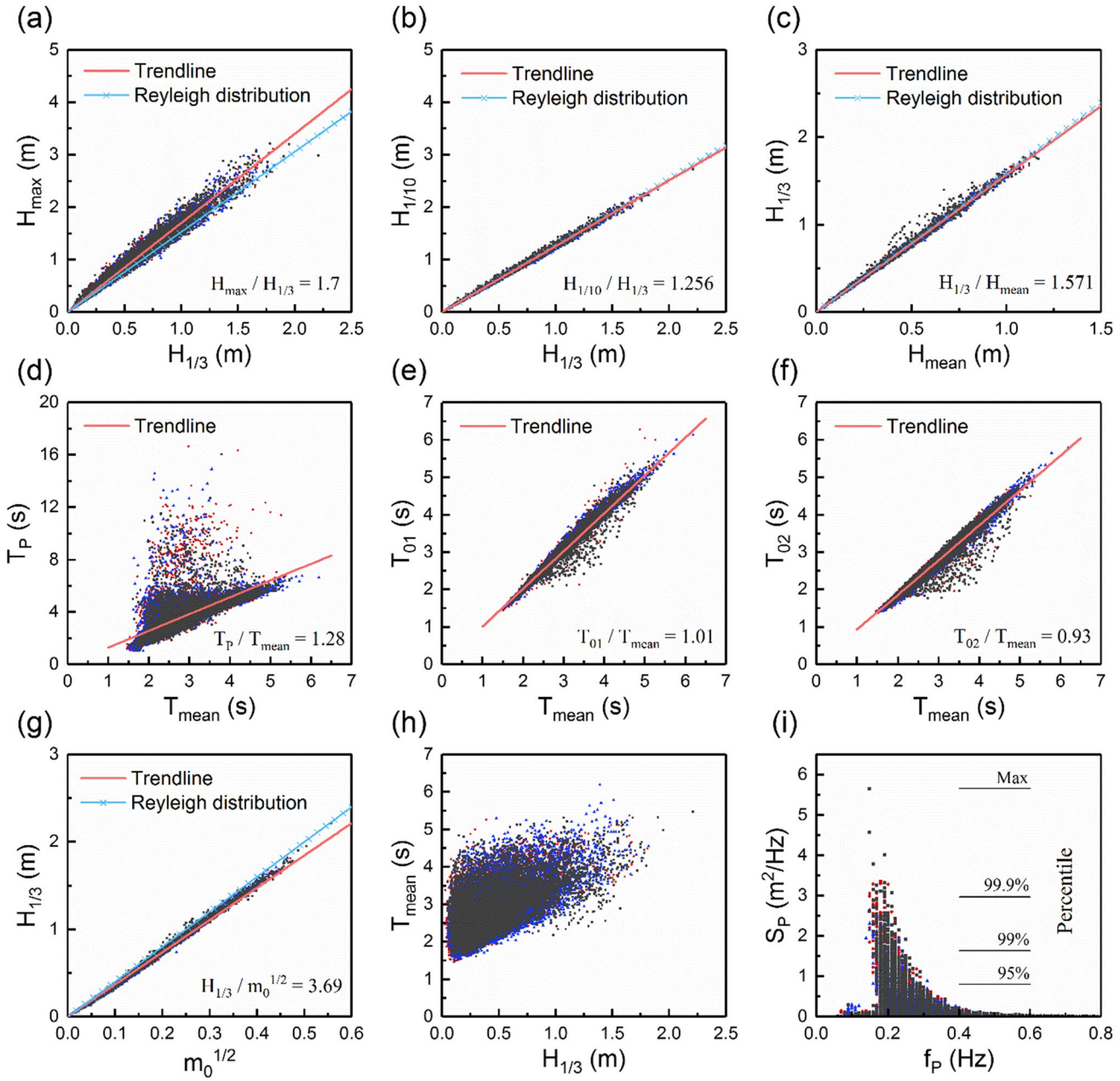


**Fig. 16** Correlation between key wave parameters. The total data in this study are displayed as scatters using different symbol colors, i.e., W1 in red, W2 in blue, and W3 in black

a similar bay area, and the results indicate a general risk for such form of coastlines.

The analysis of wave periods shows that $T_{mean}$ has an apparent correlation with spectrum-based wave periods ($T_{01}$, $T_{02}$, and $T_p$), as shown in Fig. 16e and f. The regression analysis show that, in Hangzhou Bay, $T_{mean}$ can be well replaced by $T_{01}(\approx 1.01T_{mean})$ if only spectral information is available, while the value of $T_{02}(\approx 0.93T_{mean})$ is relatively smaller and less reliable. Comparatively, the correlation between $T_{mean}$ and $T_p$ is much poorer with a large quantity of scatters (see Fig. 16d), suggesting the randomness of individual large waves.

In addition, the peak energy density is further analyzed and displayed in Fig. 16i. It is found that most of the high-energy peaks are concentrated around 0.2 Hz, which is in accord with the previous findings for wave features during extreme weather. The energy density of over 95% of spectral peaks is lower than 1 $m^2/Hz$, which is about 1/3 of the value for the 99.9th percentile group. This relationship may provide a practical guidance for engineering design and

evaluation in this region if the probability of risk is a major concern.

## 9 Summary and conclusions

East China and the East China Sea are under the influence of the East Asian monsoon, with an apparent seasonal pattern, i.e., E-SE winds in summer and NW-NE winds in winter. The wave features near the coastline also vary accordingly. The wind wave pattern in this region is significantly different from other major monsoon systems around the world, e.g., Indian monsoon or Australian monsoon. Besides, the tropical cyclones generated in the Pacific Northwest impact East China frequently with tremendous power. In recent years, a large number of offshore projects are being initiated in Hangzhou Bay due to the fast economic development and the urgent need for more clean energy. As a unique funnel-shaped semi-enclosed region bordering the East China Sea in the west, Hangzhou Bay shows different wave patterns from open oceans. These factors make it necessary and urgent to advance our existing knowledge about the wave features in this region. In this paper, we analyze the characteristics of waves observed in the middle of Hangzhou Bay using 3-year-long datasets of real-time wave profiles. Another dataset of continuous wind speed recorded at 10 m above the sea level is also provided to investigate the wind wave relationship more extensively. Statistical analysis is performed to present the annual wave distribution, the variation in different seasons, the spectral features and composition, and the growth-decay process of waves during extreme weather. In addition, more discussions are also made in terms of the joint distribution and correlation between key wave parameters. The main conclusions include the following:

1. The datasets show the detailed range of key wave parameters, including wave heights (e.g., $H_{1/3}$, $H_{\max}$), wave periods (e.g., $T_{\text{mean}}$, $T_P$), wind and wave directions, and spectral parameters (e.g., energy density distribution). It is found that larger wave heights and spectral energy density can be found in the south of the monitored area. The measured directions of wind and waves are not aligned as in open water due to deflection of the wind by the land terrain. The predominant wave directions are ENE-SE that concurs with the summer monsoon. However, the largest spectral energy density was observed in the northwest, indicating that the cold airs in winter are usually stronger than the southeasterly in summer. This conclusion is also supported by the probability rose charts of $H_{1/3}$, which show a significant proportion of large waves ($H_{1/3} > 1.0$ m) from the northwest.
2. Distinct seasonal wave patterns are caused by the prevalence of cold airs in winter and the southeasterly/typhoons in summer. The monthly variations of key wave parameters (e.g., $H_{1/3}$ and $T_{\text{mean}}$) also differ observably between different locations. In summer (e.g., June to September), the wave heights and periods measured at the three stations were generally close and varied consistently. However, both wave heights and periods in the north (W1) were significantly lower than other sites during persistent NW-NE winds, which are attributed to the fetch restriction. The occurrence probability of large waves ($H_{1/3} > 1.0$ m) in winter is much greater towards the south of the bay, but there is no significant difference in summer. Despite the frequent visits of tropical cyclones, the influence of cold winds on the overall wave climate is greater due to their persistency and strength. In general, the site-specific land proximity and monsoonal tendency are essential factors determining seasonal wave distributions in such a confined water.
3. A large proportion (> 80%) of total waves observed in Hangzhou Bay had single-peak spectra. The most typical narrow single-peak spectra were observed during extreme weather with the peak frequency of about 0.2 Hz. During the winter monsoon, the peak energy density and spectral width were generally correlated with the measurement location, i.e., less energy density and less spectral width in the north of the bay (W1). This trend concurs with the seasonal distribution of wave heights and periods mentioned above. The composition of observed waves (i.e., the ratio of local wind waves versus swells) did not vary significantly with season or month. The observed swells were mainly young swells generated in the surrounding sea areas, and thus, the mean periods of wind waves and swells are similar. For large waves ($H_{1/3} > 1.0$ m), the prevalence of wind waves and the single-peak mode are highly correlated, with both proportions higher than 90%.
4. The wave characteristics during extreme weather are analyzed for three typhoons and one strong cold wave. The wave generation processes of typhoons and cold waves generally followed the same pattern (e.g., growth-decay period, wave parameters, wind wave directions), although the meteorological origins are completely different. Compared with wave heights and periods, two other ratios (i.e., the proportions of wind waves and single-peak spectra) are therefore more suitable for indicating the impact of typhoons. We identified 0.2 Hz as the characteristic frequency of extreme waves in Hangzhou Bay, and this value can be used as a criterion for engineering practices.
5. The height-period joint distribution shows that most of the waves (70 ~ 80%) observed in this study fall within the range of $H_{1/3} = 0.1$ s ~ 1.0 s and $T_{\text{mean}} = 2 \sim 4$ s.

Large and long waves ($H_{1/3} > 1.0$ m and $T_{mean} > 4$ s) that are usually damaging had a very low probability of occurrence (2.38%). The kernel density plot shows that most of the data are concentrated in the region for $H_{1/3} < \overline{H_{1/3}}$ and $T_{mean} < \overline{T_{mean}}$, while the spreading of the scatters is generally symmetric with larger $H_{1/3}$ and $T_{mean}$. For the cumulative probability of $H_{1/3}$ and $T_{mean}$, the performance of Rayleigh and Weibull distributions is not significantly different, indicating that the shallow water effect in central Hangzhou Bay is not obvious.

6. The correlations between key wave parameters are analyzed. Compared with theoretical values for open water, extreme waves (e.g., $H_{max}$) in Hangzhou Bay are amplified by the energy concentration due to the funnel-shaped inlet. In contrast, the significant wave height ($H_{1/3}$) that is more commonly used tends to be smaller than the theoretical value obtained from spectral analysis, because of the terrain-induced energy dissipation. The correlations between wave heights or wave periods are generally significant without much deviation. Most of the high-density spectral peaks occurred around $f_P = 0.2$ Hz, but over 95% of total waves were observed with a spectral peak density lower than 1 $m^2$/Hz and a much larger mean peak frequency. It is suggested that the risk of extreme waves in the bay is usually minor.

Regarding future research, it is noticed that more studies can be conducted to investigate the wave characteristics (especially those in extreme weather) in the entire Hangzhou Bay and the detailed interacting mechanism between wind waves, swells, and topographic features, using both field data and modeling results. Besides, more attention can be paid to the interaction between waves, current, and tidal bores, which involves a highly complex coupling mechanism.

**Notation** $f_P$: Peak frequency of wave spectrum; $H_{1/3}$: Significant wave height with 1/3 exceedance probability; $H_{1/10}$: Wave height with 1/10 exceedance probability; $H_{max}$: Maximum wave height; $m_0$ : Zeroth-order moment of wave spectrum; $m_{01}$: First-order moment of wave spectrum; $m_{02}$: Second-order moment of wave spectrum; $S$ : Spectral energy density; $S_{max}$: Maximum spectral energy density; $S_P$ : The energy density of spectral peak; $T_{mean}$ =: Mean wave period; $T_P$ : Peak wake period, $T_P$=1/$f_P$; $T_{max}$: Extreme wave period with 10% exceedance probability; $T_{01} = \frac{m_0}{m_1}$: Wave period estimated using the first-order moment $m_{01}$; $T_{02} = \sqrt{\frac{m_0}{m_2}}$: Wave period estimated using the second-order moment $m_{02}$; $T_+$: The growth period of a wave process; $T_-$: The decay period of a wave process; $\nu = \sqrt{\frac{m_0 m_2}{m_1^2} - 1}$: Spectral width

**Acknowledgements** The authors would like to thank the Second Institute of Oceanography of Ministry of Natural Resources of China for providing the data used in this study. The contributions of Mr. Graham Macky and the anonymous reviewers to improving the quality of this paper are highly appreciated.

**Funding** A portion of this work is supported by the Open Fund of the Key Laboratory for Technology in Rural Water Management of Zhejiang Province (No. U ZJWEU-RWM-20200102B) and the National Natural Science Foundation Young Scientist Fund of China (No. 51709091).

## References

Amrutha MM, Kumar VS, Sharma S, Singh J, Gowthaman R, Kankara RS (2015) Characteristics of shallow water waves off the central west coast of India before, during and after the onset of the Indian summer monsoon. Ocean Eng 107:259–270

Amrutha, M.M., Kumar, V.S., 2017. Characteristics of high monsoon wind-waves observed at multiple stations in the eastern Arabian Sea. Ocean Science Discussions, 1–30.

Anoop TR, Kumar VS, Shanas PR (2014) Spatial and temporal variation of surface waves in shallow waters along the eastern Arabian Sea. Ocean Eng 81(2):150–157

Battjes JA, Groenendijk HW (2000) Wave height distributions on shallow foreshores. Coast Eng 40(3):161–182

Birch, R., Fissel, D. B., Borg, K., Lee, V., & English, D., 2004. The capabilities of Doppler current profilers for directional wave measurements in coastal and nearshore waters. In Oceans' 04 MTS/IEEE Techno-Ocean'04 (IEEE Cat. No. 04CH37600) (Vol. 3, pp. 1418–1427). IEEE.

Chun H, Suh KD (2018) Estimation of significant wave period from wave spectrum. Ocean Eng 163:609–616

Coastal Engineering Research Center., 1984. Shore protection manual. USA Department of the Army, Waterways Experiment Station, Corps of Engineers, Coastal Engineering Research Center.

George, V and Kumar, V.S., 2019. Wind-wave measurements and modelling in the shallow semi-enclosed Palk Bay. Ocean Engineering, 189, p.106401.

Glejin J, Kumar VS, Nair TB (2013) Monsoon and cyclone induced wave climate over the near shore waters off Puducherry, south western Bay of Bengal. Ocean Eng 72:277–286

Goda, Y., 1974. New wave pressure formulae for composite breakwaters. Proc. 14th Int. Conf. Coastal Engrg, Copenhagen, pp, 1702–1720.

Goda, Y., 2000. Random seas and design of maritime structures. World Scientific Pub Co Inc.

Chakrabarti SK (2005) Handbook of Offshore Engineering, Vol-1. Elsevier, Ocean Engineering Series

Holthuijsen LH (2007) Waves in oceanic and coastal waters. Cambridge University Press

Hasselmann K, Barnett TP, Bouws E, Carlson H, Cartwright DE, Enke K, Ewing JA, Gienapp H, Hasselmann DE, Kruseman P, Meerburg A (1973) Measurements of wind-wave growth and swell decay during the Joint North Sea Wave Project (JONSWAP). Erganzungsheft Zur Deutschen Hydrographischen Zeitschrift A8(12):95

Huang, B., Ren, Q., Cui, X., Wan, T., Zhang, C., Zhu, B., & Ding, H. 2021. Wave characteristics and spectrum for Pingtan Strait Bridge location. Ocean Engineering, 219, 108367.

Karmpadakis, I., Swan, C. and Christou, M., 2020. Assessment of wave height distributions using an extensive field database. Coastal Engineering, 157, p.103630.

Kumar VS, George J, Joseph D (2020) Hourly maximum individual wave height in the Indian shelf seas—its spatial and temporal variations in the recent 40 years. Ocean Dyn 70(10):1283–1302

Kumar VS, Johnson G, Dora GU, Chempalayil SP, Singh J, Pednekar P (2012) Variations in nearshore waves along Karnataka, west coast of India. J Earth Syst Sci 121(2):393–403

Kumar VS, Singh J, Pednekar P et al (2011) Waves in the nearshore waters of northern Arabian Sea during the summer monsoon. Ocean Eng 38:382–388

Li Y, Pan DZ, Chanson H, Pan CH (2019) Real-time characteristics of tidal bore propagation in the Qiantang River Estuary, China, recorded by marine radar. Cont Shelf Res 180:48–58

Liang B, Liu X, Li H, Wu Y, Lee D (2016) Wave climate hindcasts for the Bohai Sea, Yellow Sea, and East China Sea. J Coastal Res 32(1):172–180

Longuet-Higgins MS (1952) On the statistical distribution of the heights of the sea waves. J Mar Res 11(3):245–266

Mai S, Wilhelmi J, Barjenbruch U (2011) Wave height distributions in shallow waters. Coast Eng Proc 1:63

Nair MA, Kumar VS (2017) Wave spectral shapes in the coastal waters based on measured data off Karwar, west coast of India. Ocean Sci 13:365–378

Oliveira TC, Neves MG, Fidalgo R, Esteves R (2018) Variability of wave parameters and Hmax/Hs relationship under storm conditions offshore the Portuguese continental coast. Ocean Eng 153:10–22

Pedersen, T., Lohrmann, A., Krogstad, H.E., 2005. Wave measurements from a subsurface platform. Proceedings waves 2005, Madrid, Spain.

Pedersen, T., Nylund, S., Dolle, A., 2002. Wave height measurements using acoustic surface tracking. Proceedings Oceans 2002, Biloxi: Mts/ieee, 1747–1754.

Pedersen, T. and Siegel, E., 2008. Wave measurements from subsurface buoys. In 2008 IEEE/OES 9th Working Conference on Current Measurement Technology (pp. 224–233). IEEE.

Pierson WJ, Moskowitz L (1964) A proposed spectral form for fully developed wind seas based on the similarity theory of S.A. Kitaigorodskii Journal of Geophysical Research 69:5181–5190

Portilla J, Ocampo-torres FJ, Monbaliu J (2009) Spectral partitioning and identification of wind sea and swell. J Atmos Oceanic Tech 26:117–122

Ru RZ, Jiang SL (1985) A sketch of the wave in Hangzhou Bay. Donghai Marine Sci 3(2):34–40 ( in Chinese)

Ruzzo C, Saha N, Arena F (2019) Wave spectral analysis for design of a spar floating wind turbine in Mediterranean Sea. Ocean Eng 184:255–272

Sandhya KG, Remya PG, Balakrishnan Nair TM, Arun N (2016) On the co-existence of high-energy low-frequency waves and locally-generated cyclone waves off the Indian east coast. Ocean Eng 111148–154. https://doi.org/10.1016/j.oceaneng.2015.10.055

Shanas PR, Aboobacker VM, Albarakati AMA, Zubier KM (2017) Superimposed wind-waves in the Red Sea. Ocean Eng 138:9–22

Shanas PR, Aboobacker VM, Zubier KM, Albarakati AMA (2018) Spectral wave characteristics along the central coast of eastern Red Sea. Arab J Geosci 11(5):90

Soares CG, Carvalho AN (2012) Probability distributions of wave heights and periods in combined sea-states measured off the Spanish coast. Ocean Eng 52:13–21

Suh KD, Kwon HD, Lee DY (2010) Some statistical characteristics of large deepwater waves around the Korean Peninsula. Coast Eng 57:375–384

Tao AF, Yan J, Pei Y, Zheng JH, Nobuhito M (2017) Swells of the East China Sea. Journal of Ocean University of China 16(4):674–682

Wu Y, Randell D, Christou M, Ewans K, Jonathan P (2016) On the distribution of wave height in shallow water. Coast Eng 111:39–49

Xiong, J., You, Z.J., Li, J., Gao, S., Wang, Q. and Wang, Y.P., 2020. Variations of wave parameter statistics as influenced by water depth in coastal and inner shelf areas. Coastal Engineering, p.103714.

Xu Z, Nandasena NAK, Whittaker CN, Melville BW (2018) Numerical modelling of flow in Little Pigeon Bay due to the 2016 Kaikoura tsunami. Ocean Eng 159:228–236

Yang B, Shi WY, Ye Q, Zhang ZL, Yang WK, Song ZK (2017) Characteristics of waves in coastal waters of northeast Zhoushan Island during typhoons. Adv Water Sci 28(1):106–115 ( in Chinese)

Yang B, Feng WB, Zhang Y (2014) Wave characteristics at south part of radial sand ridges of Southern Yellow Sea. China Ocean Engineering 28(3):317–330

Zhao, Y.L., Yang, Y.Z., You, X.B., Liu T.J., 2012. Wind-wave characteristics in the Bohai Sea, the Yellow Sea and the East China Sea: a numerical study of cold wave event. International Conference on Remote Sensing, Environment and Transportation Engineering. IEEE, 1–5.

Zhou, Y., Ye, Q., Shi, W., Yang, B., Song, Z. and Yan, D., 2020. Wave characteristics in the nearshore waters of Sanmen bay. Applied Ocean Research, 101, p.102236.